

4. GEOCHEMISTRY OF SERPENTINITE MUDS AND METAMORPHIC ROCKS FROM THE MARIANA FOREARC, ODP SITES 1200 AND 778–779, SOUTH CHAMORRO AND CONICAL SEAMOUNTS¹

Ivan P. Savov,² Steve Guggino,² Jeffrey G. Ryan,² Patricia Fryer,³
and Michael J. Mottl⁴

ABSTRACT

New geochemical data on serpentinite muds and metamorphic clasts recovered during Ocean Drilling Program Legs 195 (Holes 1200A–1200E) and 125 (Holes 778A and 779A) provide insights into the proportions of rock types of various sources that compose the serpentinite mudflows and the fluid-rock interactions that predominate in these muds. We interpret the metamorphic rock fragments as derivatives of mostly metamorphosed mafic rocks from the descending Pacific oceanic crust. Based on their mid-ocean-ridge basalt (MORB)-like Al_2O_3 , TiO_2 , CaO , Si/Mg , and rare earth element (REE) systematics, these metamorphic rocks are classified as metabasalts/metagabbros and, therefore, ~30-km depths represent an active subduction zone setting. The serpentinite muds from Holes 1200A and 1200E have slightly lower REE when compared to Hole 1200D, but overall the REE abundance levels range between 0.1–1 × chondrite (CI) levels. The chondrite-normalized patterns have $[\text{La}/\text{Sm}]_{\text{N}} \sim 2.3$ and $[\text{Sm}/\text{Yb}]_{\text{N}} \sim 2$. With the exception of one sample, the analyzed metamorphic clasts show flat to slightly depleted light REE patterns with 1.0–15 × CI levels, resembling MORBs. Visually, ~6 vol% of the serpentinitized muds are composed of “exotic” materials

¹Savov, I.P., Guggino, S., Ryan, J.G., Fryer, P., and Mottl, M.J., 2005. Geochemistry of serpentinite muds and metamorphic rocks from the Mariana forearc, ODP Sites 1200 and 778–779, South Chamorro and Conical Seamounts. In Shinohara, M., Salisbury, M.H., and Richter, C. (Eds.), *Proc. ODP, Sci. Results*, 195, 1–49 [Online]. Available from World Wide Web: <http://www-odp.tamu.edu/publications/195_SR/VOLUME/CHAPTERS/103.PDF>. [Cited YYYY-MM-DD]

²Department of Geology, University of South Florida—Tampa, 4202 East Fowler Avenue, SCA 528, Tampa FL 33620-5201, USA. Correspondence author: savovi@si.edu

³Hawaii Institute of Geophysics and Planetology, School of Ocean and Earth Science and Technology, University of Hawaii at Manoa, 1680 East-West Road, POST 602B, Honolulu HI 96822, USA.

⁴Department of Oceanography, University of Hawaii at Manoa, 1000 Pope Road, Marine Sciences Building, Honolulu HI 96822, USA.

Initial receipt: 10 January 2004

Acceptance: 12 July 2004

Web publication: 24 February 2005
Ms 195SR-103

(metamorphic clasts [schists]). Our mixing calculations confirm this result and show that the serpentinite muds are produced by additions of ~5% metamafic materials (with flat and up to $10 \times$ CI REE levels) to serpentinitized peridotite clast material (with very low REE abundances and U-shaped chondrite-normalized patterns). The preferential incorporation of B, Cs, Rb, Li, As, Sb, and Ba into the structure of H_2O -bearing sheet silicates (different than serpentine) in the Leg 125 and Leg 195 metamorphic clasts (chlorite, amphibole, and micas) have little effect on the overall fluid-mobile element (FME) enrichments in the serpentinite muds (average B = ~13 ppm; average Cs = ~0.05 ppm; average As = ~1.25 ppm). The extent of FME enrichment in the serpentinitized muds is similar to that described for the serpentinitized peridotites, both recording interaction with fluids very rich in B, Cs, and As originating from the subducting Pacific slab.

INTRODUCTION

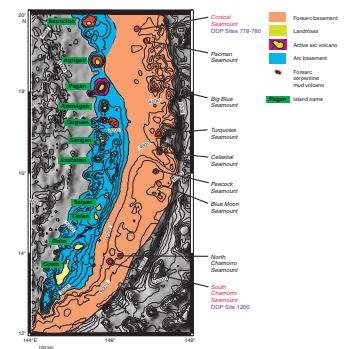
The Mariana system contains numerous large mud volcanoes composed principally of unconsolidated flows of serpentinite mud and serpentinitized mantle peridotites, along with minor amounts of clasts of metabasic rock clasts (Johnson, 1992; Maekawa et al., 1992, 1993; Fryer et al., 1999; Guggino et al., 2002). The serpentinite muds were likely formed as fault gouge during tectonic deformation of the underlying forearc mantle, resulting in unconsolidated silt- to clay-sized serpentinite sediments that migrate as a result of gravitational instability to the surface through faults and fractures in the forearc crust (Fryer, Pearce, Stokking, et al., 1992; Fryer et al., 1995). Based on earthquake locations, the estimated depth to the subducting Pacific plate under the South Chamorro and Conical seamounts is ~30 km, and the metamorphic schists recovered from the sampled forearc sites likely originated from the décollement zone as entrained clasts within the upwelling serpentinite muds (Fryer et al., 1999). We will explore the geochemical influences that metabasic rocks from the subducting slab, through dehydration and low-temperature metamorphism, may have on the trace element and fluid-mobile element systematics of the extensively studied serpentinite muds and pore fluids as the muds and fluids rise through the mantle wedge and the forearc crust.

The discovery of metamorphic schists containing Na-rich amphiboles (indicating pressures = 5 kbar) in the grit-sized fraction of the serpentinite mud from Site 1200 (Salisbury, Shinohara, Richter, et al., 2002; Gharib et al., 2002) provides strong evidence for the deep (slab) origin of the muds that are actively protruding at the summit knoll of South Chamorro Seamount (for a more detailed discussion see Fryer et al., submitted [N1]). Unlike Conical Seamount, where only two metamorphic fragments were found in six holes drilled, South Chamorro Seamount provides a significant proportion of metabasites that allow the investigation of the paragenesis of the slab-derived lithologic fraction.

REGIONAL GEOLOGY

The Izu-Bonin-Mariana (IBM) arc system extends for ~2800 km from near Tokyo, Japan, to south of Guam, Mariana Islands (Fig. F1), where the Mesozoic Pacific plate is being subducted west-northwestward be-

F1. Map of the Mariana forearc serpentinite mud volcanoes, p. 14.



neath the West Philippine plate. The Mariana forearc region preserves a record of extensive vertical movements resulting from seamount collision and fracturing associated with the arc configuration and plate motions over time (Fryer, Pearce, Stokking, et al., 1992). The forearc basement of the IBM system (Fig. F1) was formed after the initiation of “infant” arc volcanism and is a consequence of either the trapping of old, most probably Philippine Sea oceanic crust or by intra-oceanic island arc rifting and volcanism (DeBari et al., 1999; Stern et al., 2004). Initial subduction began in the early Eocene almost simultaneously for the Mariana and the Izu-Bonin segments of the IBM. This is evidenced by the eruption of boninite and arc-tholeiite lavas on Chichi Jima and Bonin Islands (Bloomer, 1983; Stern et al., 2004).

Currently, the absolute velocities of subduction along the Mariana margin are ~40 mm/yr in a northwestward direction (Stern et al., 2004, and references therein). The Pacific plate descends beneath the West Philippine plate at an angle of ~20° to depths of 60 km, whereas, at depths >100 km it dramatically steepens (to near-vertical descent in the Marianas) (Fryer, Pearce, Stokking, et al., 1992). Based on evidence from multichannel seismic reflection data, Mrozowski et al. (1981) (in the Marianas) and Horine et al. (1990) (in the Izu-Bonin) proposed that only minor sediment accretion has occurred along the entire convergent margin. The lithology of the dredged samples from the slopes of the Mariana Trench (e.g., island arc tholeiites and boninites) suggests that almost no sediment or oceanic crustal accretion occurs along the Mariana margin as well (Bloomer, 1983; Fryer, Pearce, Stokking, et al., 1992).

Ocean Drilling Program (ODP) Leg 125 Sites 778 and 779 are located on the flanks of Conical Seamount (Fig. F1) (detailed descriptions can be found in Fryer, Pearce, Stokking, et al., 1992, and in Fryer et al., 1999). Site 1200 is situated on the summit knoll of South Chamorro Seamount (Fig. F1), known as a site combining active blueschist mud volcanism and associated megafaunal assemblages (Fryer and Mottl, 1997; Salisbury, Shinohara, Richter, et al., 2002). The site is ~90 km west of the Mariana Trench axis, and based on the recent subduction rate and dip of the Pacific plate underneath the Philippine plate, the part of the Pacific crust that lies directly underneath the seamount today was located at the trench ~2.5 m.y. ago (95 km of Pacific crust been subducted to a depth of 30 km at the current ~40 mm/yr subduction rate).

Several cores were drilled on the summit and flanks of South Chamorro Seamount. Hole 1200A was cored with the rotary core barrel (RCB) to a depth of 147.2 meters below seafloor (mbsf), and serpentinitized ultramafic clasts with minor amounts of the host serpentinite matrix were recovered. Holes, 1200D, 1200E, and 1200F were cored using the advanced piston corer/extended core barrel (APC/XCB) to a maximum depth of 54.4 mbsf. The recovered soft serpentinite matrix contains metamorphic rock clasts, including blueschists (Fryer et al., 1999). Based on the presence of epidote and Na amphiboles (Gharib et al., 2002) and on similarities in the mineral paragenesis and mineral chemistry of the metabasalts studied by Maekawa et al. (1992, 1993), Gharib et al. (2002) characterized Leg 195 metabasic samples as recording low temperatures (<300°C) and high pressures.

ANALYTICAL METHODS

A suite of 41 serpentinite muds was analyzed onboard the *JOIDES Resolution* using the JY 2000 inductively coupled plasma–atomic emission spectrometer (ICP-AES). Another suite of 22 serpentinite mud samples, along with 14 of the larger metamorphic clasts from South Chamorro and Conical Seamounts, was analyzed for major and some trace elements using a direct coupled plasma–atomic emission spectrometer (DCP-AES) at the University of South Florida (USF), Tampa, Florida (USA). Sample digestions for major and some trace elements (Cr, Ni, V, Co, Sc, Zn, Cu, Sr, Ba, and Mn) were performed on LiBO₂ fluxed fusions, followed by DCP-AES measurements at USF. Concentrations of the elements of interest were accurate within ~10%, based on monitoring of replicates of certified U.S. Geological Survey (USGS) standards: DTS-1, BIR-1, AGV-1, and G-2.

Lithium abundances were measured by DCP-AES following HF:HClO₄ (4:1) sample digestion using the procedures of Ryan and Langmuir (1987). All Li determinations were performed by the standard addition method, using a gravimetric Li standard made from 99.999% pure Li₂CO₃. Reproducibility obtained for Li determinations was ±5% down to 1 ppm Li. Boron abundances were measured in 17 serpentinite mud and 12 metamorphic schist samples at USF by DCP-AES following a Na₂CO₃ fluxed fusion in Pt crucibles, a method modified from that of Ryan and Langmuir (1993) in that, as a final step, all solutions were neutralized with ultra-pure HNO₃ and no column preconcentration procedures were used. Because the majority of the measured serpentinite muds and all of the metamorphic clasts have boron abundances >10 ppm, DCP-AES reproducibility for all samples was ±5%.

A subset of serpentinite muds and metamorphic clasts were analyzed for rare earth elements (REE)—Y, Sr, Li, Be, Rb, Cs, Pb, As, Sb, U, Th, Nb, Ta, Hf, Zr, Sc, V, Ga, Cu, and Zn—at the VG Elemental PlasmaQuad II ICP-mass spectrometer (MS) facility at the Department of Earth Sciences of Boston University, Boston, Massachusetts (USA). Samples were digested in HNO₃:HF (3:1) mixtures, following procedures described by Kelley et al. (2003). Gravimetric calibration standards were matrix-matched to sample solutions by adding ~150 ppm Mg from a 1000-ppm Mg standard solution (SPEX, Metuchen, New Jersey). Based on replicate analyses of the certified standards JB-3, BIR-1, AGV-1, JP-1, and DTS-1, reproducibility was about ±2% for all of these elements. Accuracy was about ±5% for higher-concentration elements and about ±10% for the lowest-concentration elements such as As, Sb, and Be.

SAMPLE DESCRIPTIONS

The analyzed samples are metamorphic clasts and serpentine muds collected onboard the *JOIDES Resolution* during Legs 125 (Site 778 and 779, Conical Seamount) and 195 (Site 1200, South Chamorro Seamount). Examination of several impregnated serpentinite mud thin sections under cross-polarized light and smear slide analysis reveals that the muds contain abundant mineral grains, different from serpentine, and, less commonly, entire lithic fragments containing more than one mineral. Onboard X-ray diffraction analysis, as well as onshore electron microprobe analysis (Gharib et al., 2002) of the serpentinite muds confirms that Leg 195 muds contain mostly serpentine but also minerals

like brucite, chlorite, amphiboles, micas, spinel, carbonates, pyroxene, talc, and epidote (Salisbury, Shinohara, Richter, et al., 2002; Fryer et al., submitted [N1]). A detailed description of the Leg 125 serpentine mud mineralogy is given by Fryer and Mottl (1992), Lagabrielle et al. (1992), and Benton (1997). The similarities (and differences) between the Leg 125 and Leg 195 muds is discussed by Fryer and Salisbury (this volume).

A quantity of wash-core material was recovered from Hole 1200B. We wet-sieved a portion of this material using 60- μm mesh sieves and dried the sample in an oven for several hours at 100°C. Then the material was further sieved to separate the >0.1-cm fraction. The largest fraction included lithic material, mineral fragments, and crystals (mostly fibrous serpentine vein filling material) that ranged from 0.1 to ~2 cm in size (grit). The discovered metamorphic clasts are usually sub-rounded and millimeter size to a few centimeters in diameter (Fig. F2A, F2B). The grit was inspected under a binocular microscope and handpicked for discrete lithologies. Material processed for whole-rock analysis was 0.5–2 cm in diameter.

Mineralogical investigation of the larger clasts from Leg 125 shows that they are metabasalts, recording prehnite-pumpellyite to greenschist facies metamorphism (Johnson, 1992). Leg 195 metabasic lithologies include a mineralogically diverse suite of schists: chlorite/serpentine schist, sodic-amphibole/mica schist (Fig. F2C), tremolite/chlorite schist (Fig. F2B), and less common talc (Fig. F2A) and chlorite-pyroxene schists (Salisbury, Shinohara, Richter, et al., 2002; Gharib et al., 2002). Recent study of the Leg 195 metabasic clasts, as well as previous studies on Leg 125 metabasic clasts (Maekawa et al., 1992, 1993; Fryer et al., 1999), discovered high-pressure/low-temperature (HP/LT) mineral phases (Gharib et al., 2002; Fryer et al., submitted [N1]). The schists with Na amphibole composed ~1 vol% of the muds, and the proportion of metabasic grit in relation to the remaining, mostly serpentine, material is ~6 vol%. The coarse mica-schists are less abundant in Holes 1200D, 1200E, and 1200F. A predominance of chlorite-containing schists was observed in all of the holes.

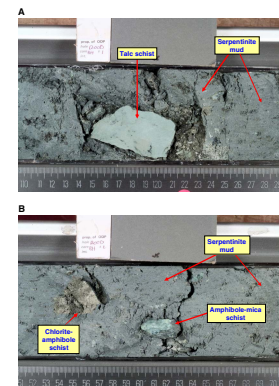
According to Johnson (1992), the non-serpentinite clasts from Leg 125 are metabasalts and metadiabases. Secondary textures usually associated with these metabasalts and metadiabases involve abundant serpentine, chlorite, carbonates, prehnite-pumpellyite, epidote, and hydrogarnets, all overprinting primary igneous textures, and less common talc, lawsonite, quartz, and Fe oxides (Johnson, 1992). In the Leg 195 metamorphic clasts, all of the primary minerals are entirely replaced by low-temperature assemblages and the primary textures of the clasts are impossible to identify. The analytical work reported in this paper is on single metamorphic (metabasic) clasts, which represent very limited amounts of sample powder. However, we have not attempted to combine or group metamorphic schists based on their similar visual appearances.

SERPENTINITE MUD GEOCHEMISTRY

Seawater-Serpentinized Peridotite Mud Interaction

Chemical interaction between the serpentinite muds and seawater was a major concern for several key elements in this study (e.g., Na, B, Sr, and K). However, the geochemistry of the pore waters indicates that

F2. Schists, p. 15.



seawater penetration is restricted to depths <5 mbsf, ruling out the likelihood of seawater contamination of the muds.

Our Leg 195 samples closely resemble those from Conical Seamount (Fryer and Mottl, 1992; Lagabrielle et al., 1992), where mixing was observed between the seawater and only the uppermost 5 m of the recovered core samples. At South Chamorro Seamount, the pore waters below depths of ~5 mbsf show stable and very high pH (always >12), high alkalinity (40–120 mmol/kg), Na/Cl ratios between 1.15 and 1.2, and high B (>3000 $\mu\text{mol}/\text{kg}$) and K (>18 mmol/kg) (for comparison, the seawater values for B and K are 420 $\mu\text{mol}/\text{kg}$ and 10.2 mmol/kg, respectively) (Mottl, 1992). Mottl et al. (2003) also observed that the South Chamorro pore waters are highly depleted relative to seawater values in Mg and Sr and have very low Li abundances (with an order of magnitude lower than the seawater). They also have an extremely fractionated Li isotope signature (~12‰ heavier than seawater) (Savov et al., 2002).

As shown by Savov et al. (2002, 2004), the serpentinized peridotites from Site 1200 have $^{87}\text{Sr}/^{86}\text{Sr} = 0.704\text{--}0.705$, with the highest $^{87}\text{Sr}/^{86}\text{Sr}$ near the top of the section and stable and consistently low $^{87}\text{Sr}/^{86}\text{Sr}$ ratios (~0.7045) for the deep samples, significantly lower than the seawater ratio ($^{87}\text{Sr}/^{86}\text{Sr} = 0.709$). These values are similar to the $^{87}\text{Sr}/^{86}\text{Sr}$ ratio of serpentinized peridotites and corresponding pore waters from Leg 125, Conical Seamount (Haggerty and Chaudhuri, 1992; Savov et al., 2002, 2004).

Near the seafloor, high-alkalinity/low-Ca deep fluids interact with the low-alkalinity/high-Ca seawater. The result is the well-documented precipitation of needlelike (centimeter sized) aragonite crystals within the serpentinite muds. This process is best recorded in the CaCO_3 content of the serpentine muds. At core depths of ~2 mbsf, CaCO_3 concentrations are elevated and may reach as high as 36 wt%, whereas below ~5 mbsf, CaCO_3 concentrations drop to consistent values <1 wt% (Salisbury, Shinohara, Richter, et al., 2002). The presence or absence and relative abundance of aragonite crystals was also used to estimate approximately how deeply the seawater has penetrated below the surface of the seamount. The low abundances of Ca, Na, Sr, and Mn in the serpentinite muds (Tables T1, T2), along with visual inspections, confirms that aragonite crystals are absent below depths of ~5 mbsf.

Comparisons between Serpentine Mud Data Sets and Serpentinized Peridotites

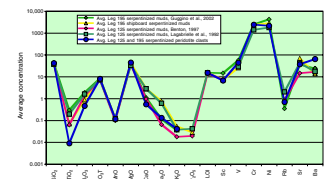
In Tables T1 and T2 we report the major and minor element abundances of the serpentinite muds. We observe several small but important differences between the compositions of the average serpentinite muds and the average serpentinized peridotites from the Mariana forearc sites (Fig. F3). Serpentine muds have higher average Al_2O_3 (0.9 wt%), CaO (1.4 wt%), and TiO_2 (0.1 wt%) (Tables T1, T2). Figure F4A shows that all of the studied serpentine muds have average loss on ignition (LOI) values similar to serpentinized peridotite clasts (ranging between 14.27 and 15.56 wt%) but higher SiO_2/MgO ratios. The Leg 195 muds and clasts have comparable SiO_2 contents (~43 wt%) but are higher in MgO relative to the muds from Leg 125 (Lagabrielle et al., 1992; Benton, 1997) (Fig. F4B, F4C).

Using Figure F4A, F4B, and F4C, we investigate relationships between LOI, MgO, and SiO_2 contents of the serpentinite muds. When

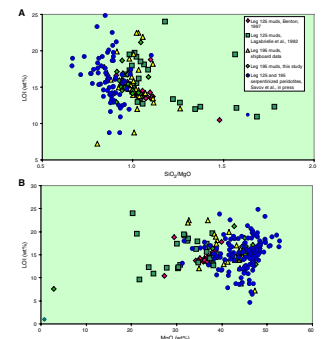
T1. ICP-AES analysis of serpentinite muds, p. 37.

T2. DCP-AES analysis of serpentinite muds, p. 41.

F3. Major and trace element compositions of serpentinite muds, p. 17.



F4. SiO_2 , MgO, and LOI, p. 18.



compared to the Leg 125 serpentinite muds of Lagabrielle et al. (1992) and Benton (1997), the Leg 195 muds contain as much as 10 wt% higher average MgO (Fig. F4B) and 4 wt% higher average SiO₂ (Fig. F4C). The Leg 195 muds also have elevated Ni concentrations (as much as 1500 ppm higher), lower Rb, and higher Cr compared to the data of Lagabrielle et al. (1992) and higher average Sr (as much as 50 ppm higher) compared to the data set of Benton (1997). When combined, the entire serpentinite mud data set (Legs 125 and 195) shows positive correlations between SiO₂/MgO ratios and TiO₂ and Al₂O₃ contents (Fig. F5A, F5B). No such correlation was observed between the SiO₂/MgO ratios and Fe₂O₃ and CaO contents (Fig. F5C, F5D). The serpentinite muds always have TiO₂ > 0.01 wt%, and in almost all cases this parameter discriminates them well from the serpentinitized peridotite clasts, which contain average TiO₂ ~ 0.01 wt%.

When compared to the hydrated ultramafic rocks (serpentinitized peridotite clasts) from Legs 125 and 195, the muds generally show lower MgO, Fe₂O₃, Ni, and Cr (Figs. F4C, F5D, F6) and elevated TiO₂, Al₂O₃, CaO, and Sr (Figs. F5A, F5B, F5C, F7A, F7B, F7C) or trends toward the compositions of altered seafloor basalts (Kelley et al., 2003) or metabasaltic clasts reported by Johnson (1992) and in this study.

Rare Earth Element Systematics

We report here the first measurements of rare earth elements (as well as Nb, Ta, Hf, Th, U, Pb, Zr, Cs, As, and Sb) in the muds from serpentinite seamounts in the Mariana forearc (Table T3). The analyzed serpentinite muds (total of 14 samples) were recovered from Leg 195 Holes 1200A, 1200D, and 1200E. Chondrite-normalized plots of REE for the serpentinite muds (Fig. F8A, F8B) show relatively flat patterns with average [La/Sm]_N = 2.3 and average [Sm/Yb]_N = 2. In Holes 1200D, 1200E, and 1200A, the [La/Sm]_N range is 0.13–1.9, 0.2–4.2, and 1.16–1.32, respectively. In Hole 1200D, the serpentinite muds exhibit slight negative Eu anomalies (Fig. F8A). In Holes 1200D, 1200E, and 1200A, the [Sm/Yb]_N range is 0.1–0.5, 0.35–1.2, and 0.3–0.4, respectively.

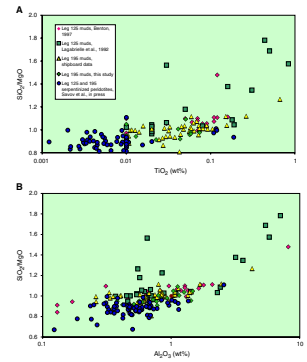
These patterns are drastically different from the relative abundances and chondrite-normalized REE patterns of the serpentinitized peridotites from Legs 125 or 195. As seen in Figure F8A and F8B, the serpentinitized peridotite clasts from Legs 125 and 195 have a noticeable positive Eu anomaly and they also never reach more than 0.1 × chondrite (CI) level (i.e., their REE abundances are a factor of 1 or 2 lower than the serpentinite muds) (see Table T3).

METAMORPHIC CLAST GEOCHEMISTRY

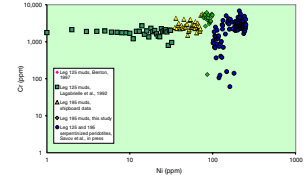
Major Elements

In Tables T4 and T5 we report major and minor element abundances of the different metamorphic rocks recovered from the serpentinite muds of Legs 125 and 195, respectively. The major and trace element geochemistry of the metamorphic clasts is highly variable (Figs. F9, F10, F11). Some samples show highly variable SiO₂ (30–65 wt%) and relatively uniform MgO (~40 wt%) (Fig. F9A), and others have uniform SiO₂ contents (~45 wt%) and highly variable MgO contents (5–45 wt%) as well as elevated CaO (Fig. F9A, F9B). Some of the high-MgO samples could be derived from the metamorphism of ultramafic protoliths. This

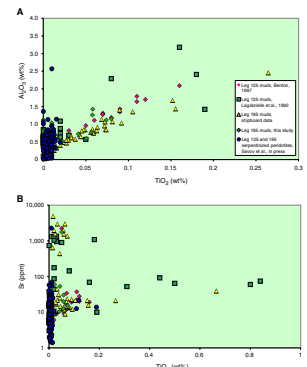
F5. SiO₂/MgO vs. TiO₂, Al₂O₃, CaO, and Fe₂O₃, p. 20.



F6. Ni vs. Cr for serpentinite muds, p. 22.

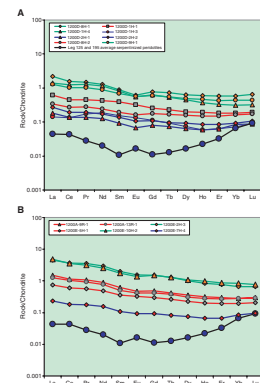


F7. TiO₂ vs. Al₂O₃, Sr, CaO, and V, p. 23.



T3. ICP-MS analysis of serpentinite muds, p. 43.

F8. Coryell-Masuda diagrams for serpentinite muds, p. 25.



is because the same samples also show elevated LOI, high Ni (average = 2280 ppm), high Cr (1040–3950 ppm), and low TiO₂ (0.04–0.4 wt%) abundances (see Table T5). However, we believe the majority of the samples are derived from mid-ocean-ridge basalt (MORB)-like protoliths because not only do they have low MgO, but they also have low LOI, Ni (average = 470 ppm), and Cr (14–340 ppm) as well as high TiO₂ (0.97–3.58 wt%) (Figs. F9C, F10C) and Al₂O₃ (Figs. F9C, F10A). Samples from this same group possess MORB-like REE patterns (see below), as well as high-field-strength element and large-ion-lithophile element abundances inconsistent with derivation from serpentinized peridotites. Moreover, the metabasic samples have Si/Mg ratios ranging from 2.1 to 8.9 (serpentinized peridotite Si/Mg ~ 1) (Figs. F10, F11). And finally, the Leg 195 metabasic samples show major and trace element systematics similar to those of metabasalt and metadiabase samples recovered from Leg 125 (Johnson, 1992).

Fluid-Mobile Elements

We analyzed 16 samples of serpentinite muds for B, Be, and Li abundances (Table T6) and several of the large schists (Fig. F2) for their trace element concentrations (Table T7). Both the serpentinite muds and the metamorphic schists have higher B, Li, and Be contents relative to unaltered depleted mantle values (~0.25 and 1.6 ppm and 25 ppb, respectively) (Ryan and Langmuir, 1987, 1993; Salters and Stracke, 2004) (Figs. F11, F12, F13). When evaluated vs. the immobile TiO₂ contents (as an approximate distinction between ultramafic and mafic protolith), boron seems to be enriched in both the high- and low-TiO₂ samples (Fig. F12). The metamorphic clasts also have higher Li concentrations compared to the serpentinite muds and serpentinized peridotite clasts (Figs. F11A, F13). The metabasic rocks from both South Chamorro and Conical Seamounts have very high B/Be (8–2715; average = 358) and B/Li (average = 2.9) in respect to the depleted mantle B/Be and B/Li values (~2 and ~0.07, respectively) (Salters and Stracke, 2004). However, on plots such as Si/Mg ratios vs. Li concentrations (Fig. F11A) and Si/Mg ratios vs. B concentrations (Fig. F11B), the high B and Li of the clasts seems to be independent of Si/Mg. In the case of boron, it seems likely that processes of low-temperature fluid-rock exchange in the upwelling materials have resulted in relatively high B contents in any rock with appropriate host phases. The abundances of other fluid-mobile elements (FME), such as As and Cs, are also elevated by orders of magnitude relative to the depleted mantle values (Fig. F13). The extent of enrichment is very interesting because even though the host lithology is different (major phases in the metamorphic clasts are chlorite, amphiboles, and micas), the patterns of enrichment in FME resemble those found for serpentinite muds and serpentinized peridotites (i.e., B, As, and Cs) are orders of magnitude enriched, followed by moderate enrichments in Li and Sb and no enrichments in Pb, Rb, Ba, Th, and U (Savov et al., 2002, in press) (Fig. F13). Further microprobe studies of the FME abundances in metamorphic minerals is needed for better understanding of the mechanism of FME transfer from fluids to appropriate forearc host minerals.

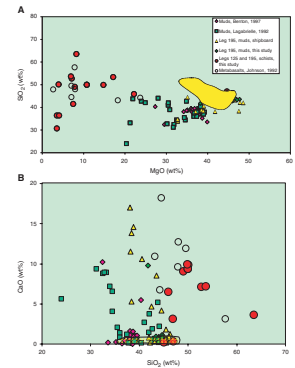
Rare Earth Element Systematics

All of the analyzed metamorphic schists exhibit flat chondrite-normalized REE patterns with ~10 × CI abundance levels, [La/Sm]_N ~ 1.3,

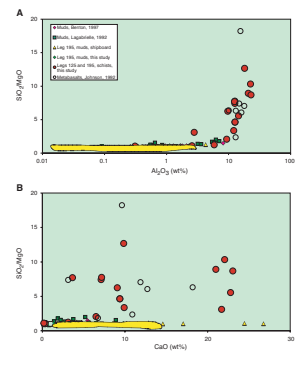
T4. DCP-AES analysis of metabasic rocks, Sites 778 and 779, p. 44.

T5. DCP-AES analysis of metabasic rocks, Site 1200, p. 44.

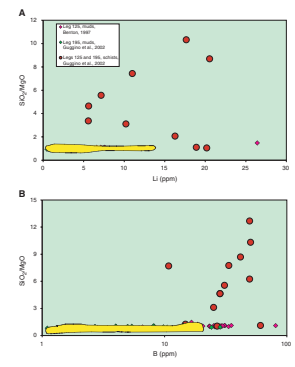
F9. SiO₂ vs. MgO and CaO, Al₂O₃ vs. TiO₂, p. 26.



F10. SiO₂/MgO vs. Al₂O₃, CaO, and TiO₂, p. 28.



F11. SiO₂/MgO vs. Li and B, p. 30.



T6. DCP-AES Boron, Be, and Li analysis of metabasic rocks, p. 46.

T7. ICP-MS analysis of metabasic rocks, p. 47.

and $[Sm/Yb]_N \sim 1.15$ (Fig. F14). These patterns are identical to earlier REE results on metabasalt samples recovered from Conical Seamount (Johnson, 1992). The Conical Seamount samples show slight light REE (LREE)-depleted patterns ($[La/Sm]_N = 0.6$), and one sample from South Chamorro Seamount shows an LREE-enriched pattern ($[La/Sm]_N = 6.3$) (Fig. F14). By comparison, the subducted sediment REE patterns from the Mariana convergent margin show LREE enrichments of up to $40 \times$ CI (Plank and Langmuir, 1998). Thus, with the exception of one sample (195-1200D-8H-1, 119–121 cm), the REE chondrite-normalized patterns and abundances confirm the inferences from the major element geochemistry and show MORB-like schist protoliths resembling those of basalts and gabbros from mid-ocean-ridge (MOR) settings. The generally mafic nature of the schist protoliths is also supported by their very low Th/Nd ratios (average = 0.054) and their very high Nb/Th ratios (average = 11.2) (Th, Nd, and Nb abundances are listed in Table T7; average Mariana Trench sediments have Th/Nd = 0.12 and Nb/Th = 4.2) (Plank and Langmuir, 1998).

DISCUSSION AND CONCLUSIONS

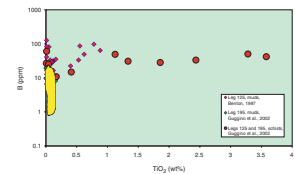
Origin of the Serpentinite Muds

The Mariana forearc region is thought to be non-accretionary (Husong, Uyeda, et al., 1981; Fryer, Pearce, Stokking, et al., 1992). The differences between the serpentine muds and the serpentinized peridotite clasts discussed earlier indicate additions of “exotic” materials to the serpentinite muds. From the similarities between the serpentinite muds and the serpentinized peridotites (Fig. F3), it is evident that the serpentinized ultramafic materials control the composition of the serpentinite muds. However, the major and trace element geochemistry of the serpentinite muds suggest the admixture of a slab (MORB-like) component. In Figure F15 we have calculated binary mixing arrays between averages of the serpentinized peridotite and metamorphic schist compositions compiled in Table T8. Interestingly, independent of element and ratios chosen, the serpentinite muds always plot on (or very close to) the mixing lines between average serpentinized peridotite and metamorphic schist compositions (Fig. F15). Moreover, their positions on Figure F15 always correspond to additions of 3%–5% metamorphic clast materials to the serpentinized peridotites.

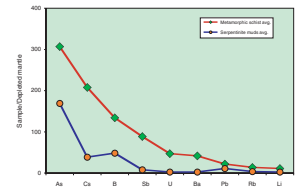
Origin of the Metamorphic Schists

The metamorphic schists incorporated in the serpentinite muds originated from a basaltic protolith, either from a trapped Philippine Sea plate or, more possibly, from the subducting Pacific slab. If the samples have Pacific plate origin, then they will be representative of the metamorphic pressure and temperature conditions existing at the slab/mantle interface and will thus be appropriate for testing the current models for mantle wedge pressure-temperature conditions postulated by Peacock (1996) and Peacock and Wang (1999). By contrast, the presence of trapped Philippine sea crust in the Mariana forearc (see De Bari et al., 1999) metamorphosed to HP/LT conditions implies that this crust was actively involved in the proto-Mariana intra-arc rifting and then tectonically emplaced to considerable depths (high pressures) in the Mariana forearc mantle. Philippine plate origin scenarios are hard to explain

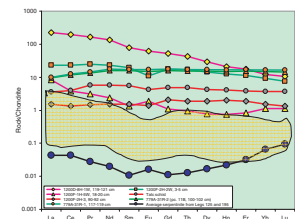
F12. TiO₂ vs. B, p. 31.



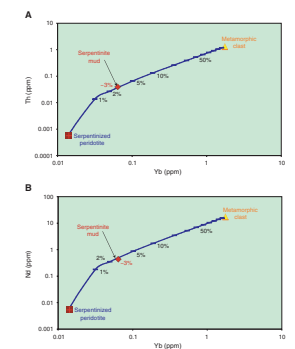
F13. Depleted mantle normalized plot of fluid-mobile elements, p. 32.



F14. Coryell-Masuda diagram for metamorphic clasts, p. 33.



F15. Mixing curves, p. 34.



T8. Selected average element concentrations, p. 48.

with the existing velocity structure of the forearc region. Hf and Nd isotopes, which are insensitive to alteration and low-temperature metamorphism, may be used in the future to distinguish between these two potential sources, as was successfully done for western Pacific samples by Pearce et al. (1999).

IMPLICATIONS FOR THE ELEMENTAL RECYCLING

As noted by Bebout (1995), Ryan et al. (1995, 1996), and Bebout et al. (1999), metamorphism at the slab/mantle interface may prevent the deep subduction of highly volatile components such as H₂O, N, B, As, Cs, and I (Snyder et al., this volume). The large but selective enrichments of fluid-mobile elements in the serpentinite muds (this study) and clasts (Savov, 2004), their distinct REE distributions, and the fractionation of B, Cs, and As from Rb, Li, Ba, Pb, and U reveal a distinctive elemental signature produced through the depletion of the subducted Mariana slab assemblage (Plank and Langmuir, 1998; Kelley et al., 2003). The mechanical mixing of mineralogically diverse metabasalt fragments with serpentinitized peridotites in the forearc mantle wedge may help explain the large B and Li isotope fractionations required to produce the isotopic oddities of various forearc mantle and slab-derived rocks (Benton et al., 2001, 2004; Savov et al., 2002; Marschall et al., 2003). The extreme enrichments of fluid-mobile elements in serpentinite muds could not be explained by simple mechanical mixing with slab-derived metamorphic schists. Because the fluid-mobile element enrichment patterns in the serpentinitized muds resemble those of serpentinitized peridotites, we suggest that they both were created by interaction with deeply derived slab fluids having very high B, As, and Cs contents.

ACKNOWLEDGMENTS

This research is part of the senior author doctoral dissertation and was funded by a Joint Oceanographic Institutions/United States Science Advisory Committee (JOI/USSAC) Leg 195 postcruise science support grant. The help of Katherine Kelley and Terry Plank, who hosted the first author and allowed full access to their ICP-MS Facility at Boston University, is appreciated. Anette Farah helped with the sample preparation and DCP-AES analysis at USF. The authors appreciate the advice and the stimulating discussions with J. Gharib, M. D'Antonio, R. King, M. Kristensen, H. Marschall, and S. Tonarini. We thank R. Stern and T. Zack for their thoughtful and constructing reviews, as well as L. Peters for editorial assistance during review of the initial manuscript. This research used samples and/or data provided by the Ocean Drilling Program (ODP). ODP is sponsored by the U.S. National Science Foundation (NSF) and participating countries under the management of Joint Oceanographic Institutions (JOI), Inc.

REFERENCES

- Bebout, G., 1995. The impact of subduction-zone metamorphism on mantle-ocean chemical cycling. *Chem. Geol.*, 126:191–218.
- Bebout, G., Ryan, J.G., Leeman, W., and Bebout, A., 1999. Fractionation of trace elements by subduction-zone metamorphism-effect of convergent-margin thermal evolution. *Earth Planet. Sci. Lett.*, 171:63–81.
- Benton, L.D., 1997. Origin and evolution of serpentine seamount fluids, Mariana and Izu-Bonin forearcs: implications for the recycling of subducted material [Ph.D. dissert.]. Univ. Tulsa.
- Benton, L.D., Ryan, J.G., and Savov, I.P., 2004. Lithium abundance and isotope systematics of forearc serpentinites, conical seamount, Mariana forearc: insights into the mechanics of slab-mantle exchange during subduction. *Geochem. Geophys. Geosyst.*, 5:10.1029/2004GC000708.
- Benton, L.D., Ryan, J.G., and Tera, F., 2001. Boron isotope systematics of slab fluids as inferred from a serpentine seamount, Mariana forearc. *Earth Planet. Sci. Lett.*, 187:273–282.
- Bloomer, S.H., 1983. Distribution and origin of igneous rocks from the landward slopes of the Mariana Trench: implications for its structure and evolution. *J. Geophys. Res.*, 88:7411–7428.
- DeBarì, S., Taylor, B., Spencer, K., and Fujioka, K., 1999. A trapped Philippine Sea plate origin for MORB from the inner slope of the Izu-Bonin Trench. *Earth Planet. Sci. Lett.*, 174:183–197.
- Fryer, P., and Mottl, M.J., 1992. Lithology, mineralogy, and origin of serpentine muds recovered from Conical and Torishima forearc seamounts: results of Leg 125 drilling. In Fryer, P., Pearce, J.A., Stokking, L.B., et al., *Proc. ODP, Sci. Results*, 125: College Station, TX (Ocean Drilling Program), 343–362.
- Fryer, P., and Mottl, M., 1997. *Shinkai* 6500 investigations of a resurgent mud volcano on the southeastern Mariana forearc. *JAMSTEC J. Deep Sea Res.*, 13:103–114.
- Fryer, P., Mottl, M., Johnson, L., Haggerty, J., Phipps, S., and Maekawa, H., 1995. Serpentine bodies in the forearcs of western Pacific convergent margins: origin and associated fluids. In Taylor, B., and Natland, J. (Eds.), *Active Margins and Marginal Basins of the Western Pacific*. Geophys. Monogr., 88:259–279.
- Fryer, P., Pearce, J.A., Stokking, L.B., et al., 1992. *Proc. ODP, Sci. Results*, 125: College Station, TX (Ocean Drilling Program).
- Fryer, P., Wheat, C.G., and Mottl, M.J., 1999. Mariana blueschist mud volcanism: implications for conditions within the subduction zone. *Geology*, 27:103–106.
- Gharib, J., Fryer, P., and Ross, K., 2002. Lithological and mineralogical analysis of serpentine mud samples from the Mariana forearc. *Eos, Trans. Am. Geophys. Union*, 83:T72A. (Abstract)
- Guggino, S., Savov, I.P., Ryan, J.G., and ODP Leg 195 Scientific Party, 2002. Light element systematics of metamorphic clasts from ODP Legs 125 and 195, S. Chamorro and Conical Seamounts, Mariana forearc. *Eos, Trans. Am. Geophys. Union*, 83:V51A-08. (Abstract)
- Haggerty, J.A., and Chaudhuri, S., 1992. Strontium isotopic composition of the interstitial waters from Leg 125: Mariana and Bonin forearc. In Fryer, P., Pearce, J.A., Stokking, L.B., et al., *Proc. ODP, Sci. Results*, 125: College Station, TX (Ocean Drilling Program), 397–400.
- Horine, R.L., Moore, G.F., and Taylor, B., 1990. Structure of the outer Izu-Bonin forearc from seismic-reflection profiling and gravity modeling. In Fryer, P., Pearce, J.A., Stokking, L.B., et al., *Proc. ODP, Init. Repts.*, 125: College Station, TX (Ocean Drilling Program), 81–94.
- Hussong, D.M., Uyeda, S., et al., 1981. *Init. Repts. DSDP*, 60: Washington (U.S. Govt. Printing Office).

- Johnson, L.E., 1992. Mafic clasts in serpentine seamounts: petrology and geochemistry of a diverse crustal suite from the outer Mariana forearc. *In* Fryer, P., Pearce, J.A., Stokking, L.B., et al., *Proc. ODP, Sci. Results*, 125: College Station, TX (Ocean Drilling Program), 401–413.
- Kelley, K.A., Plank, T., Ludden, J., and Staudigel, H., 2003. Composition of altered oceanic crust at ODP Sites 801 and 1149. *Geochem., Geophys., Geosyst.*, 4:10.1029/2002GC000435.
- Lagabrielle, Y., Karpoff, A.-M., and Cotten, J., 1992. Mineralogical and geochemical analysis of sedimentary serpentinites from Conical Seamount (Hole 778A): implication for the evolution of serpentine seamounts. *In* Fryer, P., Pearce, J.A., Stokking, L.B., et al., *Proc. ODP, Sci. Results*, 125: College Station, TX (Ocean Drilling Program), 325–342.
- Maekawa, H., Shimizu, M., Ishii, T., Saboda, K., and Ogawa, Y., 1992. Metamorphic rocks from the serpentinite seamounts in the Mariana and Izu-Ogasawara forearcs. *In* Fryer, P., Pearce, J.A., Stokking, L.B., et al., *Proc. ODP, Sci. Results*, 125: College Station, TX (Ocean Drilling Program), 415–430.
- Maekawa, H., Shozuni, M., Ishii, T., Fryer, P., and Pearce, J.A., 1993. Blueschist metamorphism in an active subduction zone. *Nature*, 364:520–523.
- Marschall, H., Altherr, R., Ludwig, T., and Kalt, A., 2003. Boron isotope study of high-pressure metamorphic rocks from Syros (Greece) by SIMS. *Geophys. Res.*, 5:05068. (Abstract)
- Mottl, M.J., 1992. Pore waters from serpentinite seamounts in the Mariana and Izu-Bonin forearcs, Leg 125: evidence for volatiles from the subducting slab. *In* Fryer, P., Pearce, J.A., Stokking, L.B., et al., *Proc. ODP, Sci. Results*, 125: College Station, TX (Ocean Drilling Program), 373–385.
- Mottl, M.J., Komor, S.C., Fryer, P., and Moyer, C.L., 2003. Deep-slab fluids fuel extremophilic Archaea on a Mariana forearc serpentinite mud volcano: Ocean Drilling Program Leg 195. *Geochem., Geophys., Geosyst.*, 4:10.1029/2003GC000588.
- Mrozowski, C.L., Hayes, D.E., and Taylor, B., 1981. Multichannel seismic reflection surveys of Leg 60 sites, Deep Sea Drilling Project. *In* Hussong, D., Uyeda, S., et al., *Init. Repts. DSDP*, 60: Washington (U.S. Govt. Printing Office), 57–69.
- Nakamura, N., 1974. Determination of REE, Ba, Fe, Mg, Na, and K in carbonaceous and ordinary chondrites. *Geochim. Cosmochim. Acta*, 38:757–776.
- Noll, P.D., Newsom, H.E., Leeman, W.P., and Ryan, J.G., 1996. The role of hydrothermal fluids in the production of subduction zone magmas: evidence from siderophile and chalcophile trace elements and boron. *Geochim. Cosmochim. Acta*, 60:587–611.
- Peacock, S.M., 1996. Thermal and petrologic structure of subduction zones. *In* Bebout, G.E., Scholl, D.W., Kirby, S.H., and Platt, J.P. (Eds.), *Subduction Top to Bottom*. Geophys. Monogr., 96:119–133.
- Peacock, S.M., and Wang, K., 1999. Seismic consequences of warm versus cool subduction zone metamorphism: examples from northeast and southwest Japan. *Science*, 286:937–939.
- Pearce, J.A., Kempton, P.D., Nowell, G.M., and Noble, S.R., 1999. Hf-Nd element and isotope perspective on the nature and provenance of mantle and subduction components in western Pacific arc-basin systems. *J. Petrol.*, 80:1579–1611.
- Plank, T., and Langmuir, C.H., 1998. The chemical composition of subducting sediment and its consequences for the crust and mantle. *Chem. Geol.*, 145:325–394.
- Ryan, J.G., and Langmuir, C.H., 1987. The systematics of lithium abundances in young volcanic rocks. *Geochim. Cosmochim. Acta*, 51:1727–1741.
- Ryan, J.G., and Langmuir, C.H., 1993. The systematics of boron abundances in young volcanic rocks. *Geochim. Cosmochim. Acta*, 57:1489–1498.
- Ryan, J.G., Morris, J., Bebout, G.E., and Leeman, W.P., 1996. Describing chemical fluxes in subduction zones: insights from ‘depth-profiling’ studies of arc and forearc rocks. *In* Bebout, G.E., Scholl, D.W., Kirby, S.H., and Platt, J.P. (Eds.), *Subduction Top to Bottom*. Geophys. Monogr., 96:263–268.

- Ryan, J.G., Morris, J., Tera, F., Leeman, W.P., and Tsvetkov, A., 1995. Cross-arc geochemical variations in the Kurile arc as a function of slab depth. *Science*, 270:625–627.
- Salisbury, M.H., Shinohara, M., Richter, C., et al., 2002. *Proc. ODP, Init. Repts.*, 195 [CD-ROM]. Available from: Ocean Drilling Program, Texas A&M University, College Station TX 77845-9547, USA.
- Salters, V., and Stracke, A., 2004. Composition of the depleted mantle. *Geochem., Geophys., Geosyst.*, 5:10.1029/2003GC000597.
- Savov, I.P., 2004. Petrology and geochemistry of subduction-related rocks from the Mariana arc-basin system [Ph.D. dissert.], Univ. South Florida, Tampa, Florida.
- Savov, I.P., Ryan, J.G., Chan, L.H., D'Antonio, M., Mottl, M., and Fryer, P., 2002. Geochemistry of serpentinites from the S. Chamorro Seamount, ODP Leg 195, Site 1200, Mariana forearc—implications for recycling at subduction zones. *Geochim. Cosmochim. Acta*, 66:A670.
- Savov, I.P., Ryan, J.G., D'Antonio, M., Kelley, K., and Mattie, P., 2004. Geochemistry of serpentinitized peridotites from the Mariana forearc–Conical Seamount, ODP Leg 125: implications for the elemental recycling at subduction zones. *Geochem., Geophys., Geosyst.*, 6(1):10.1029/2004GC000777.
- Savov, I.P., Ryan, J.G., Mattie, P., and Schijf, J., 2000. Fluid-mobile element systematics of ultramafic xenoliths from the Izu-Bonin-Mariana forearc: implications for the chemical cycling in subduction zones. *Eos, Trans. Am. Geophys. Union*, 81:V-21C-02.
- Stern, R.J., Fouch, M.J., and Klemperer, S., 2004. An overview of the Izu-Bonin-Mariana subduction factory. In Eiler, J. (Ed.), *Inside the Subduction Factory*. Geophys. Monogr., 138:175–223.

Figure F1. Map of the Mariana forearc serpentinite mud volcanoes. Note that South Chamorro Seamount (Leg 195) is almost 6° south of Conical Seamount (Leg 125). Modified from Fryer et al. (1999).

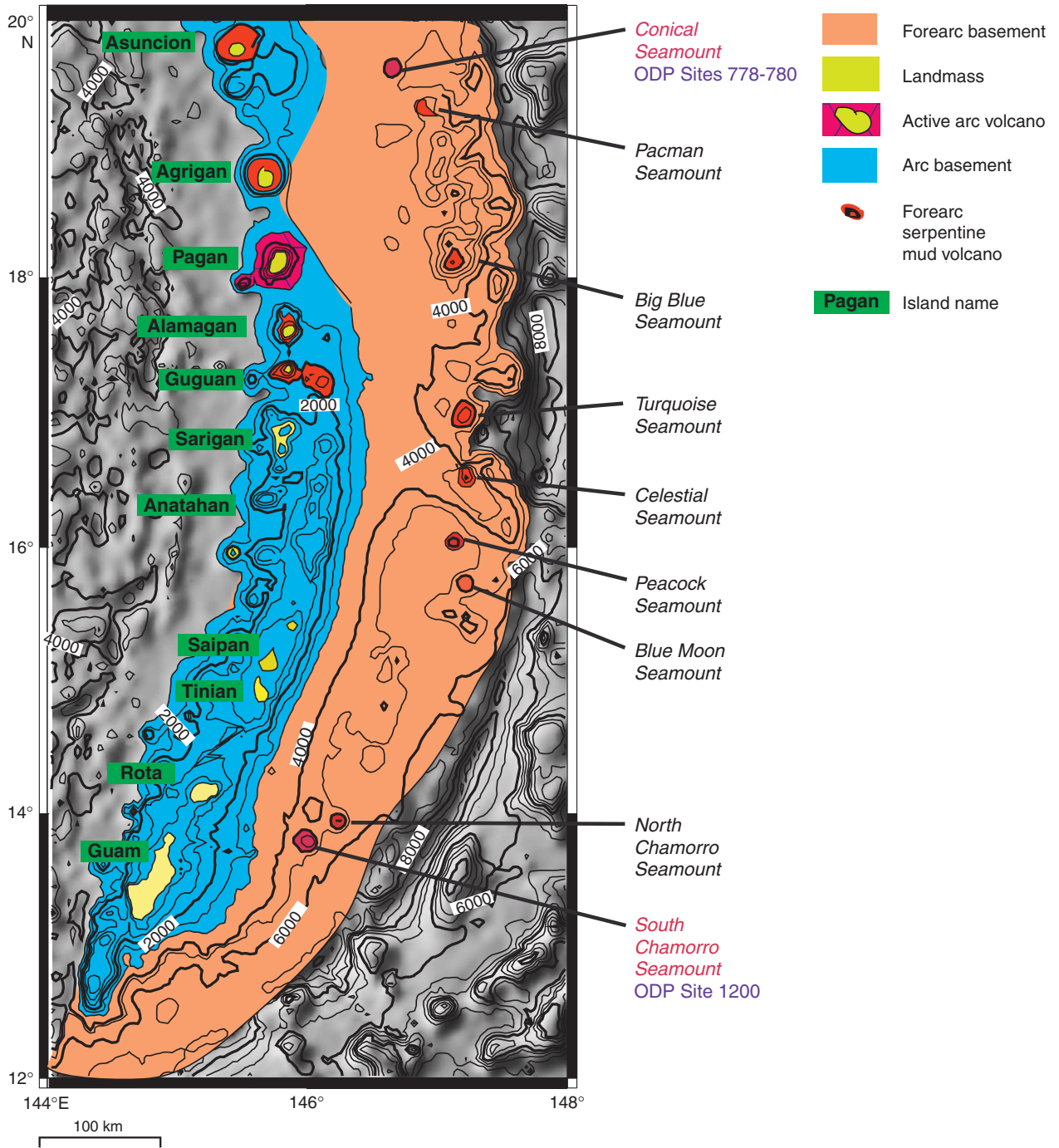
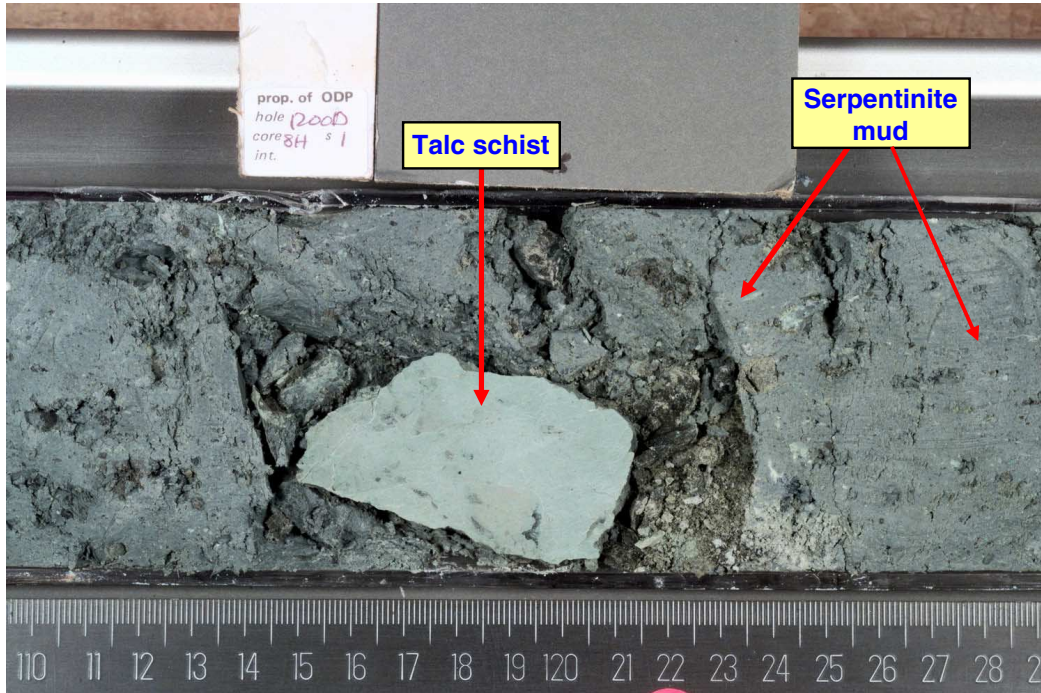


Figure F2. A. Large talc schist in serpentinite mud core (Section 195-1200D-8H-1). Scale in A and B = cm.
B. Large chlorite-amphibole (left) and amphibole-mica (right) schists in serpentinite mud core (Section 195-1200D-8H-2). (Continued on next page.)

A



B

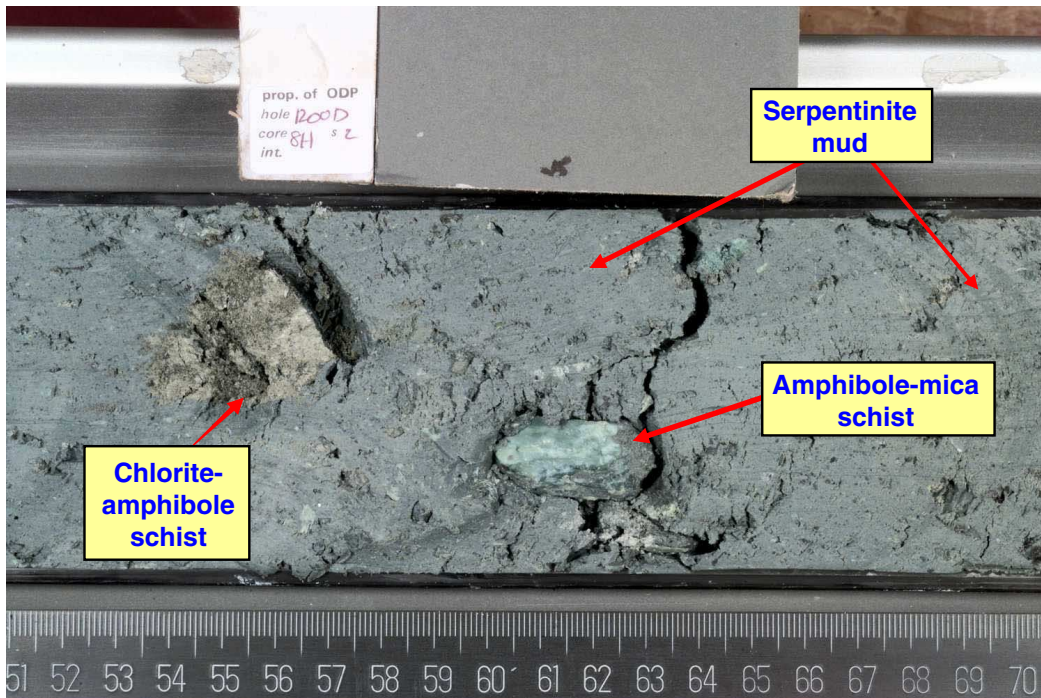
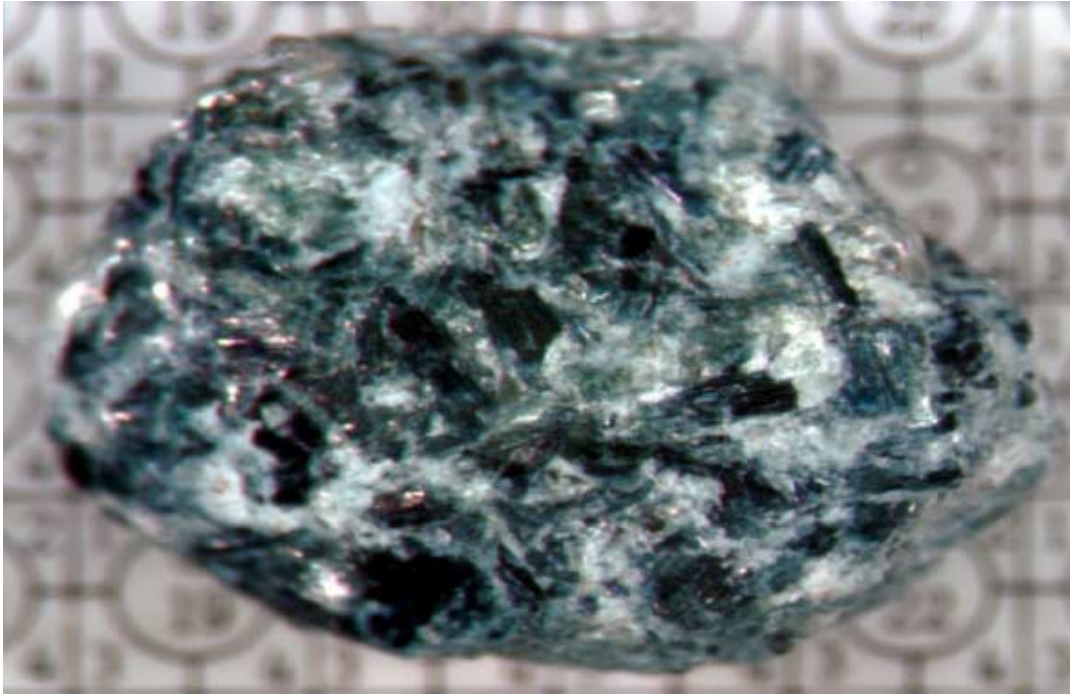


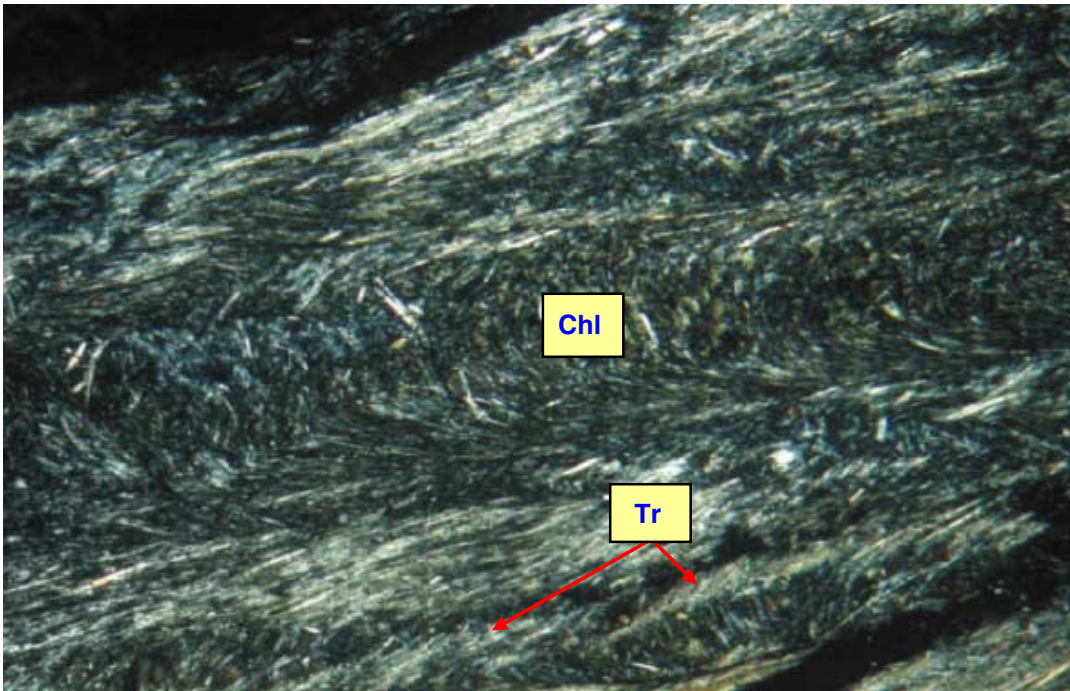
Figure F2 (continued). C. Small sodic amphibole-mica schist recovered from the Hole 1200B grit fraction. D. Cross-polarized light photomicrograph of chlorite (Chl)-tremolite (Tr) schist.

C



1 mm

D



0.5 mm

Figure F3. Comparison between the average major and some trace element compositions of serpentinite muds from ODP Legs 125 and 195. Also plotted are the average major and trace element abundances for the serpentinitized peridotites from Leg 195 (Salisbury, Shinohara, Richter, et al., 2002; Savov et al., 2002; Savov, 2004) and Leg 125 (Fryer, Pearce, Stokking, et al., 1992; Savov et al., 2000; Savov, 2004). Avg. = average. LOI = loss on ignition. Note that compared to the average serpentinitized peridotite clasts, the muds from both legs have higher TiO_2 , Al_2O_3 , and CaO (typically all with abundances of up to several weight percent in MORBs, but only trace amounts in depleted mantle peridotites). Average concentrations are given in weight percent for oxides and LOI and in parts per million for all other elements.

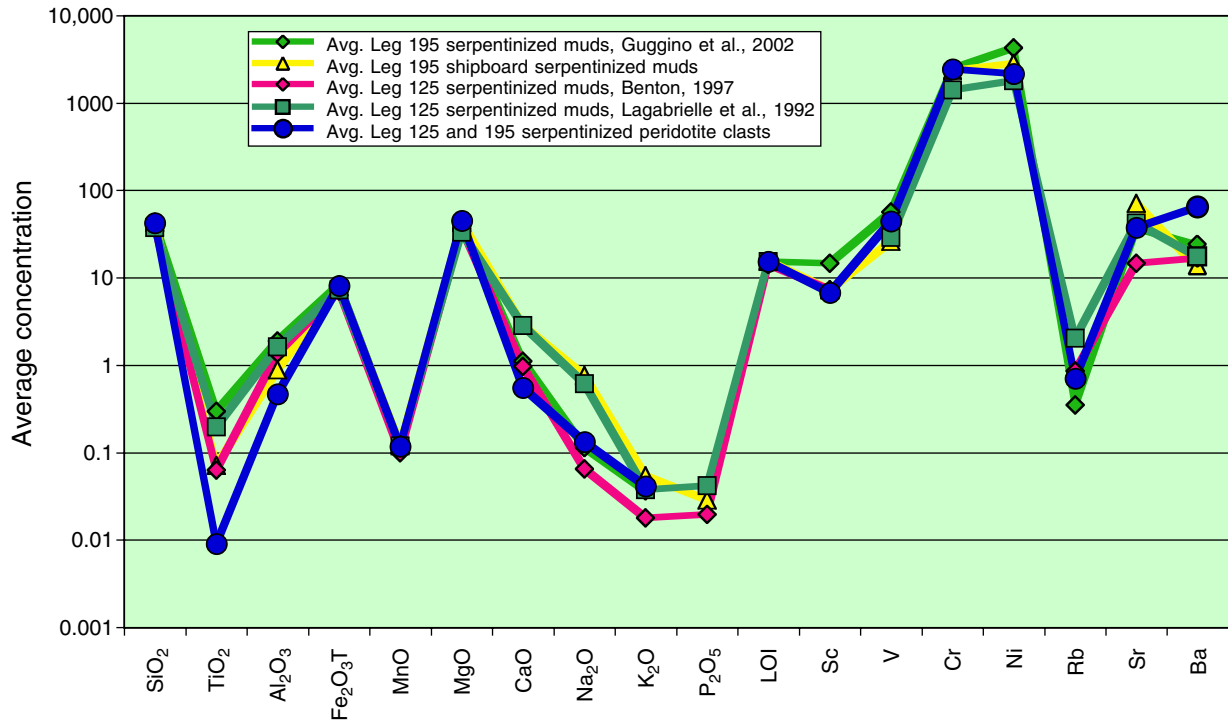


Figure F4. A. SiO_2/MgO ratio vs. loss on ignition (LOI) for serpentinite muds. For comparison we also included the ODP Legs 125 and 195 serpentinitized peridotites. The serpentinitized peridotite clasts and the serpentinite muds have similar LOI contents (average = ~15 wt%), but the SiO_2/MgO ratio of the muds is higher. Also note that the serpentinitized peridotites are usually with $\text{Si}/\text{Mg} \sim 1$. **B.** MgO vs. LOI for serpentinite muds. For comparison we also included the ODP Legs 125 and 195 serpentinitized peridotites. Overall the serpentinite muds from Leg 195 (Guggino et al., 2002, and shipboard data) have higher MgO than the Leg 125 serpentinite muds, resembling the serpentinitized peridotites. There is no relationship between the LOI and MgO in any of the data sets plotted. (Continued on next page.)

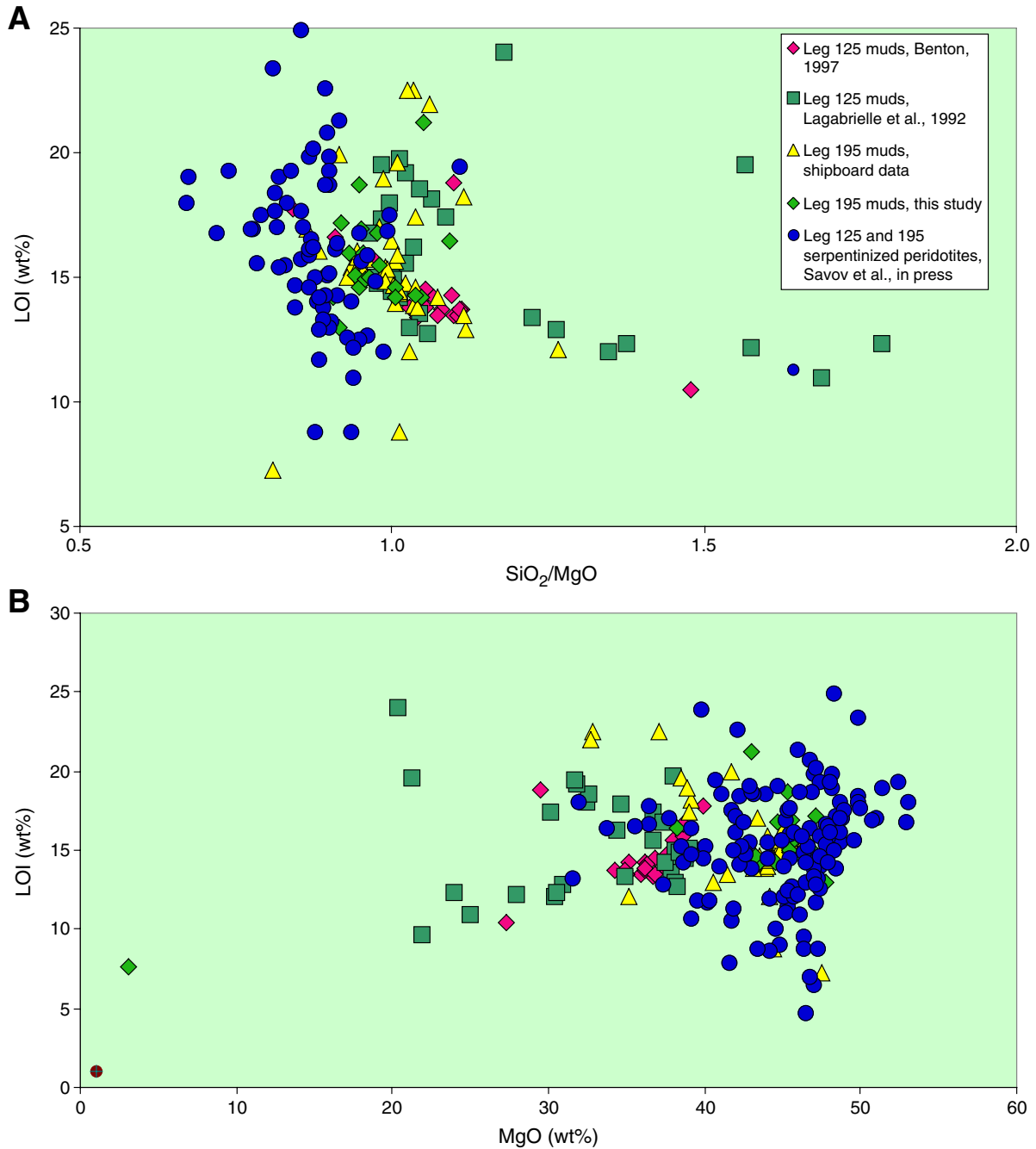


Figure F4 (continued). C. SiO₂ vs. MgO for serpentinite muds. For comparison also shown are ODP Legs 125 and 195 serpentinitized peridotites. The serpentinite muds have similar to the serpentinitized peridotites SiO₂ and lower MgO contents. In all of the samples analyzed, there is no correlation between the SiO₂ and the MgO abundances. Symbols are the same as in A. Also, symbols in Figures F4–F7 are consistent.

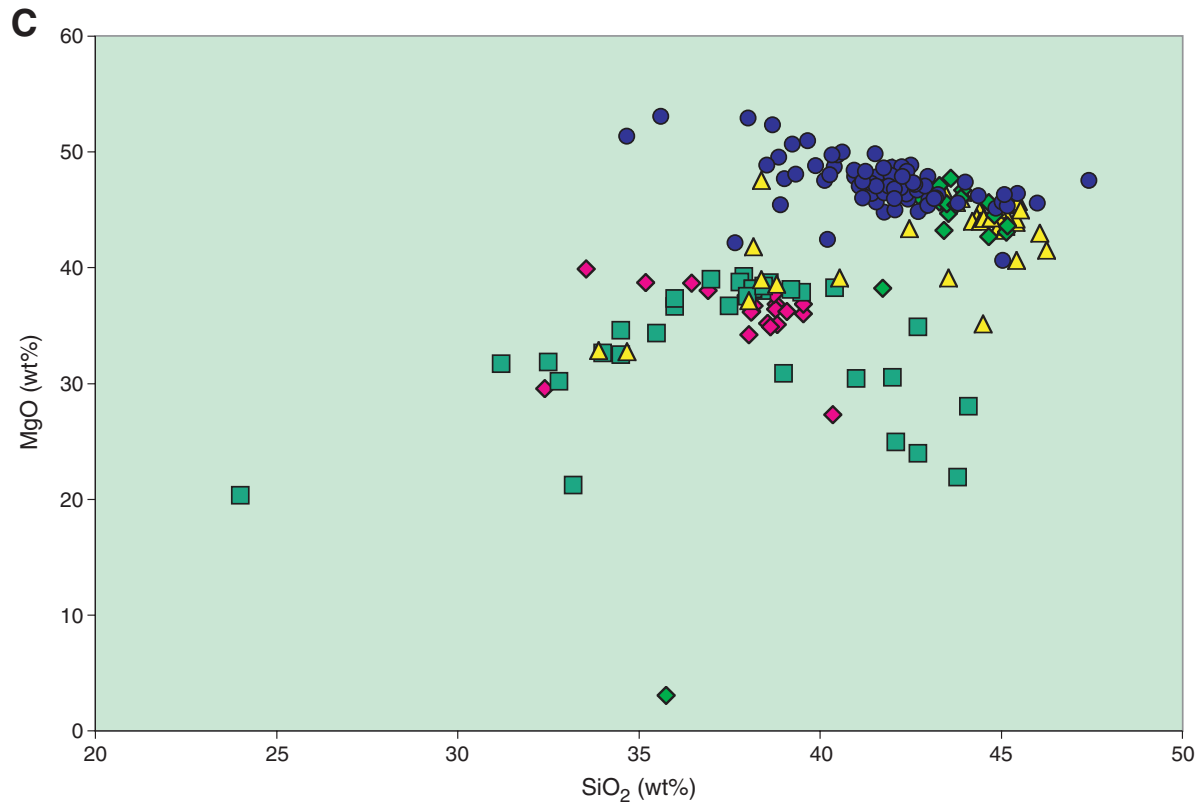


Figure F5. A. SiO_2/MgO vs. TiO_2 in serpentinite muds and ODP Legs 125 and 195 serpentinitized peridotites. The majority of the serpentinite peridotites have lower TiO_2 when compared to the serpentinite muds (the TiO_2 of the serpentinitized peridotites is always 0.01 wt%). There exists a slight positive correlation between the SiO_2/MgO and TiO_2 of the serpentinite muds. B. SiO_2/MgO vs. Al_2O_3 for serpentinite muds. When compared to the serpentinitized peridotites, the serpentinite muds from ODP Legs 125 and 195 have higher SiO_2/MgO , but many also have higher Al_2O_3 . (Continued on next page.)

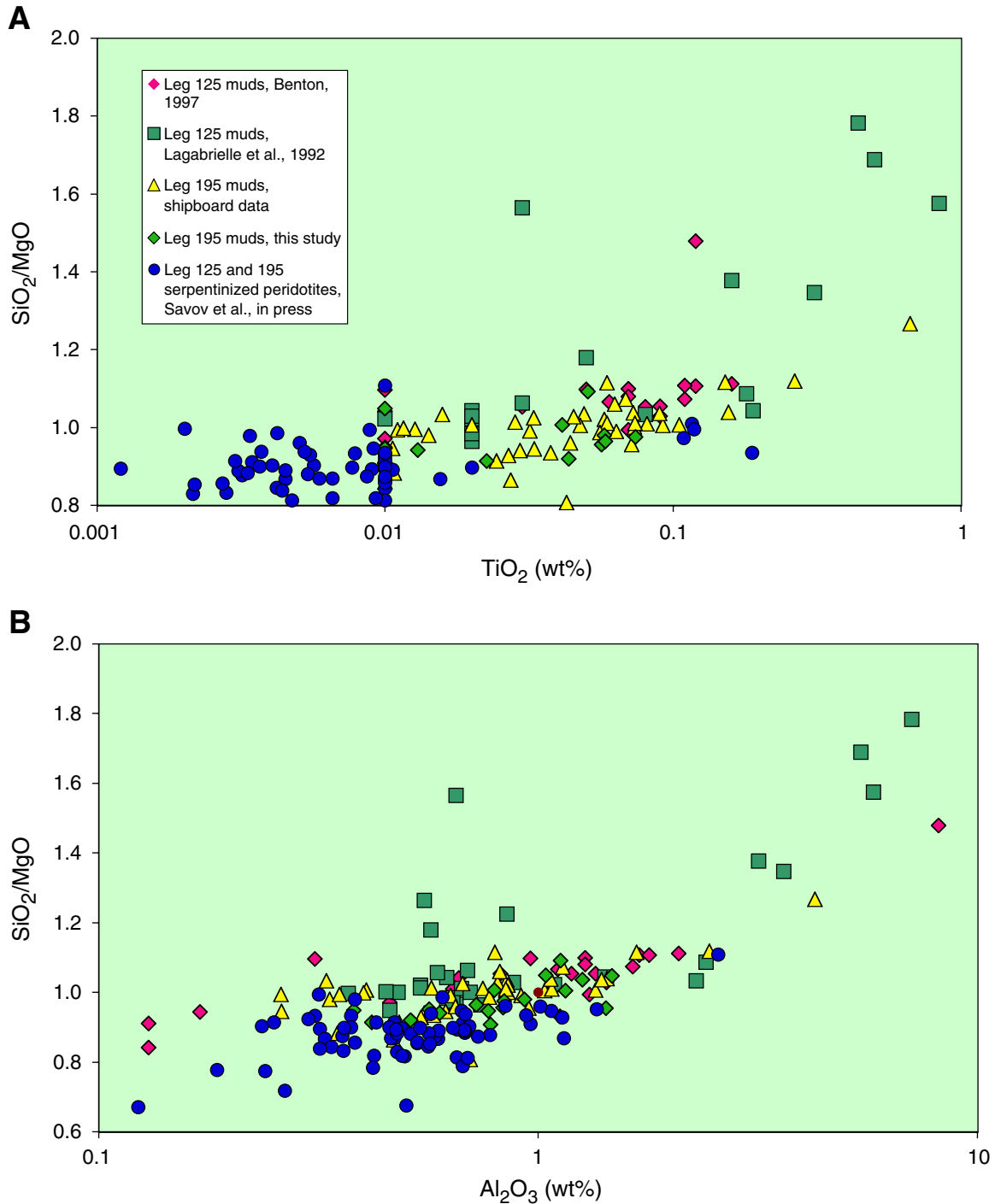


Figure F5 (continued.) C. SiO_2/MgO vs. CaO for serpentinite muds. Note that many of the serpentinite muds have higher CaO contents than the serpentinitized peridotites. Samples with very high CaO (>5 wt%) (in the shipboard and Lagabrielle et al. [1992] data sets), are samples recovered very close to the seafloor and contain aragonite crystals. Symbols are the same as in A. D. SiO_2/MgO vs. Fe_2O_3 for serpentinite muds. Note that the serpentinite muds have lower Fe_2O_3 when compared with the serpentinitized peridotites. The Leg 195 muds of Guggino et al. (2002) show the highest Fe_2O_3 contents among the serpentinite mud data sets. Symbols are the same as in A.

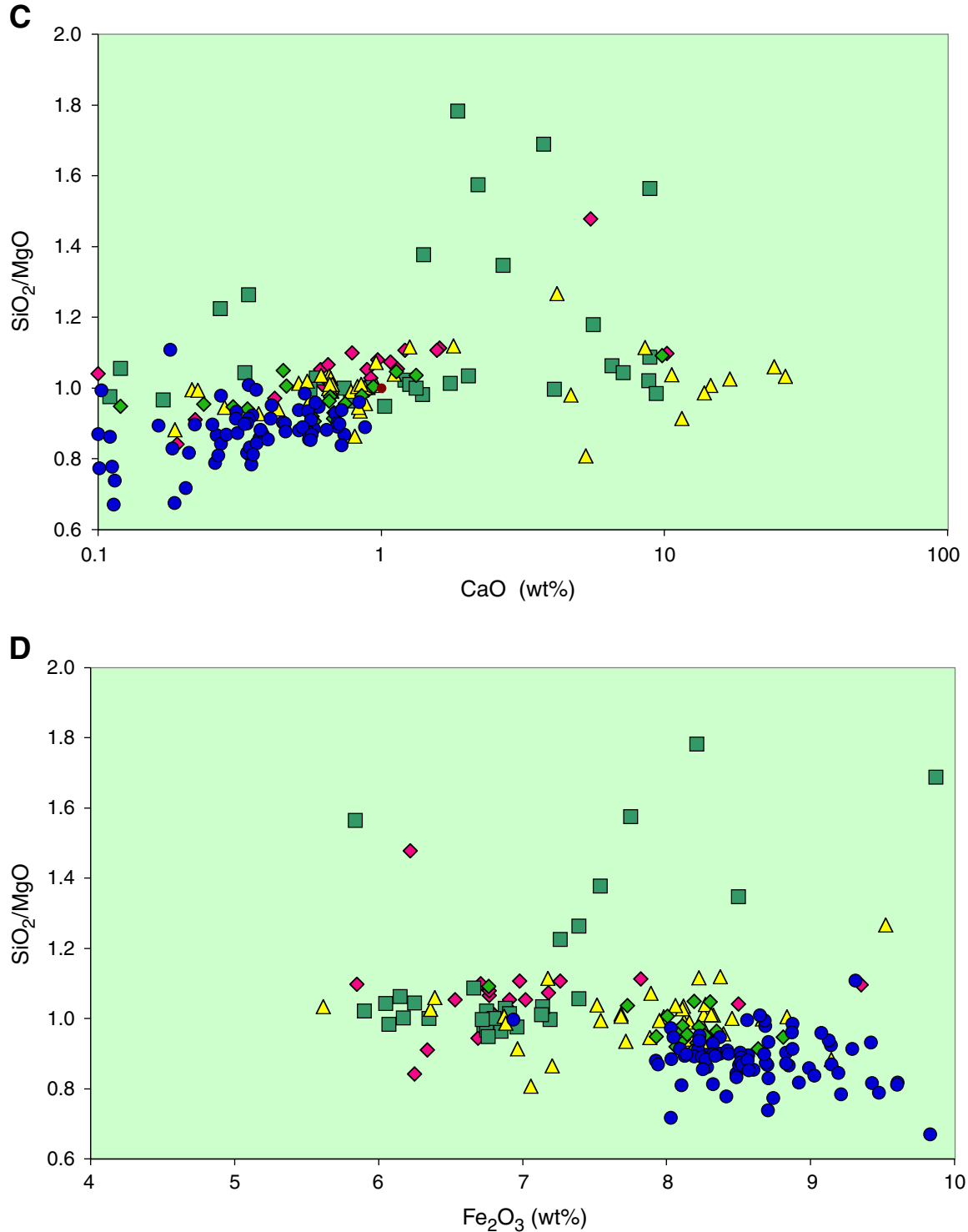


Figure F6. Ni vs. Cr for serpentinite muds. Similar to TiO_2 , there exists a clear difference between the Ni content of the serpentinite muds and the serpentinized peridotites. Although they have similar Cr contents, the measured Ni in Leg 195 muds (both shipboard data and Guggino et al., 2002) plots between the serpentinite muds from Leg 125 (Lagabrielle et al., 1992) and the serpentinized peridotites (100–250 ppm). The abundances of Ni and Cr were not measured in the serpentinite muds studied by Benton (1997).

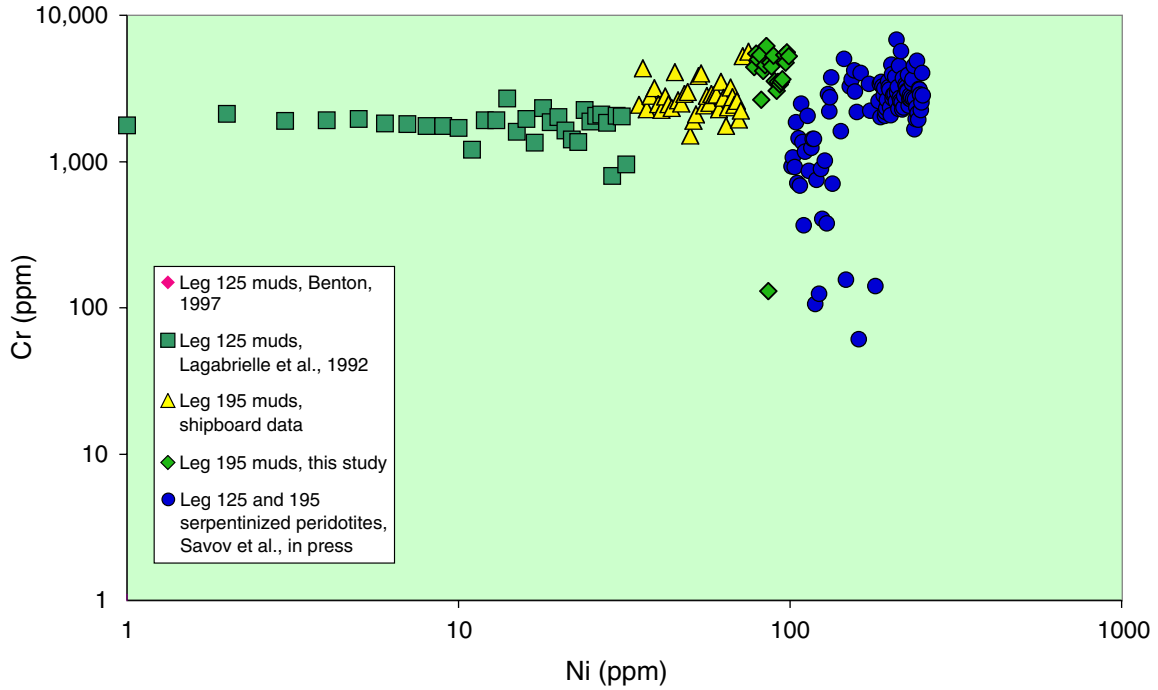


Figure F7. A. TiO_2 vs. Al_2O_3 for serpentinite muds. Note the positive correlation, especially for the Leg 195 Shipboard and Leg 125 (Benton, 1997) data sets. B. TiO_2 vs. Sr for serpentinite muds. Serpentinite mud samples with very high Sr contents (>500 ppm) were recovered from near the seafloor and correspond to the high CaO samples of Figure F5C, p. 21. There is a trend of increasing TiO_2 , whereas Sr contents remain unchanged. The Sr abundances measured in the deep serpentinite muds are similar to those of the serpentinized peridotites. (Continued on next page.)

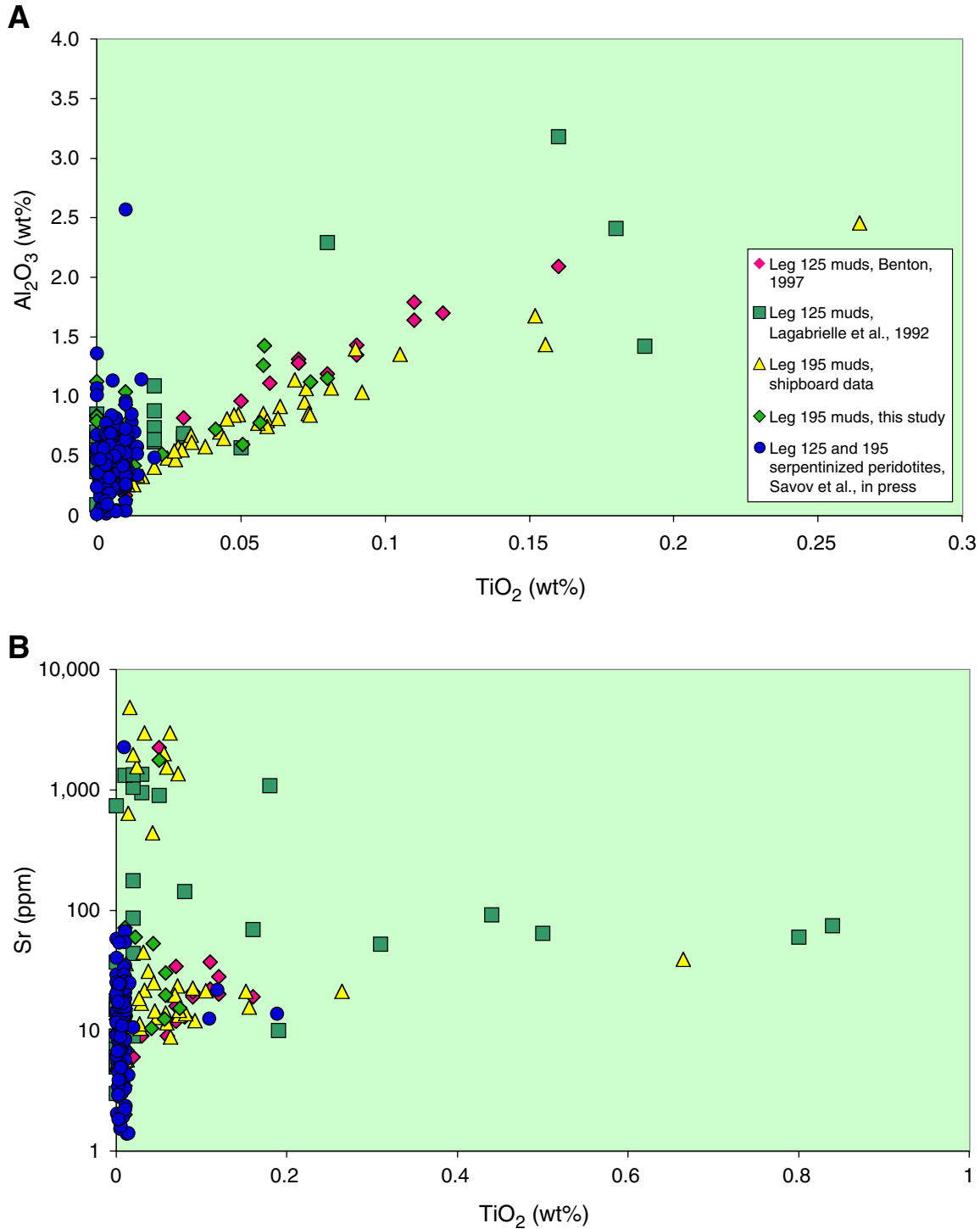


Figure F7 (continued). C. TiO_2 vs. CaO for serpentinite muds. There is no correlation between the TiO_2 and CaO contents. Abundances of $\text{TiO}_2 \sim 0.01$ wt% seem to discriminate well between the serpentine muds and serpentinitized peridotites. Symbols are the same as in A. D. TiO_2 vs. V for serpentinite muds. The Leg 195 serpentinite muds from Guggino et al. (2002) show highest vanadium and the ODP Leg 195 shipboard muds show the lowest vanadium. However, the V range in the serpentinitized peridotites (6–85 ppm) overlaps the one measured in the serpentinite muds. Symbols are the same as in A.

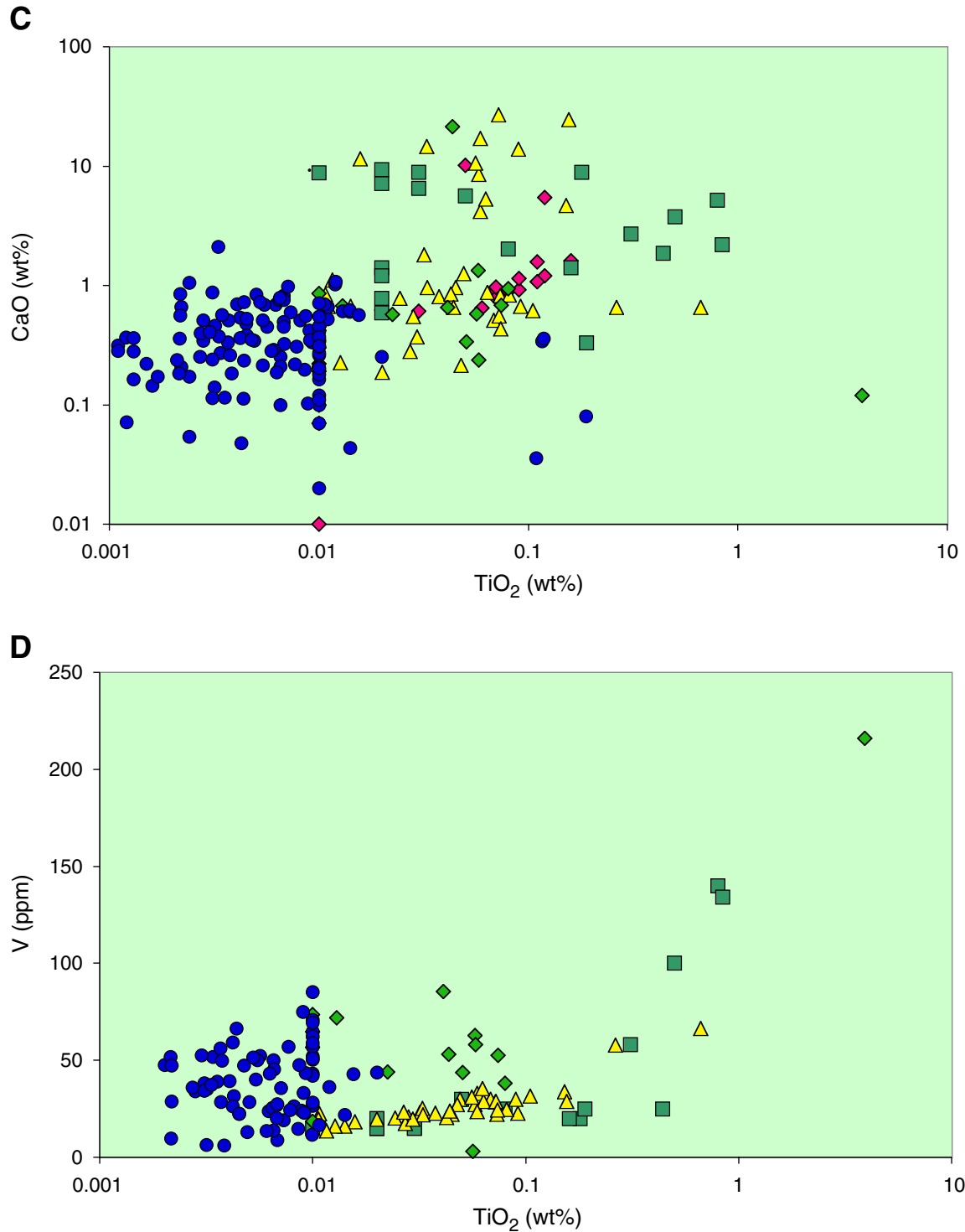


Figure F8. A. Coryell-Masuda diagram for serpentinite muds from Leg 195, Hole 1200D, normalized to chondrites (Nakamura, 1974). Note the different abundances (and patterns) between the serpentinite muds and the average serpentinitized peridotites of Savov (2004). **B.** Coryell-Masuda diagram for serpentinite muds from Leg 195, Holes 1200A and 1200E, normalized to chondrites (Nakamura, 1974). Note the different abundances (and patterns) between the serpentinite muds and the average serpentinitized peridotites of Savov (2004). Also note the REE abundances are similar to the muds from Hole 1200D (A).

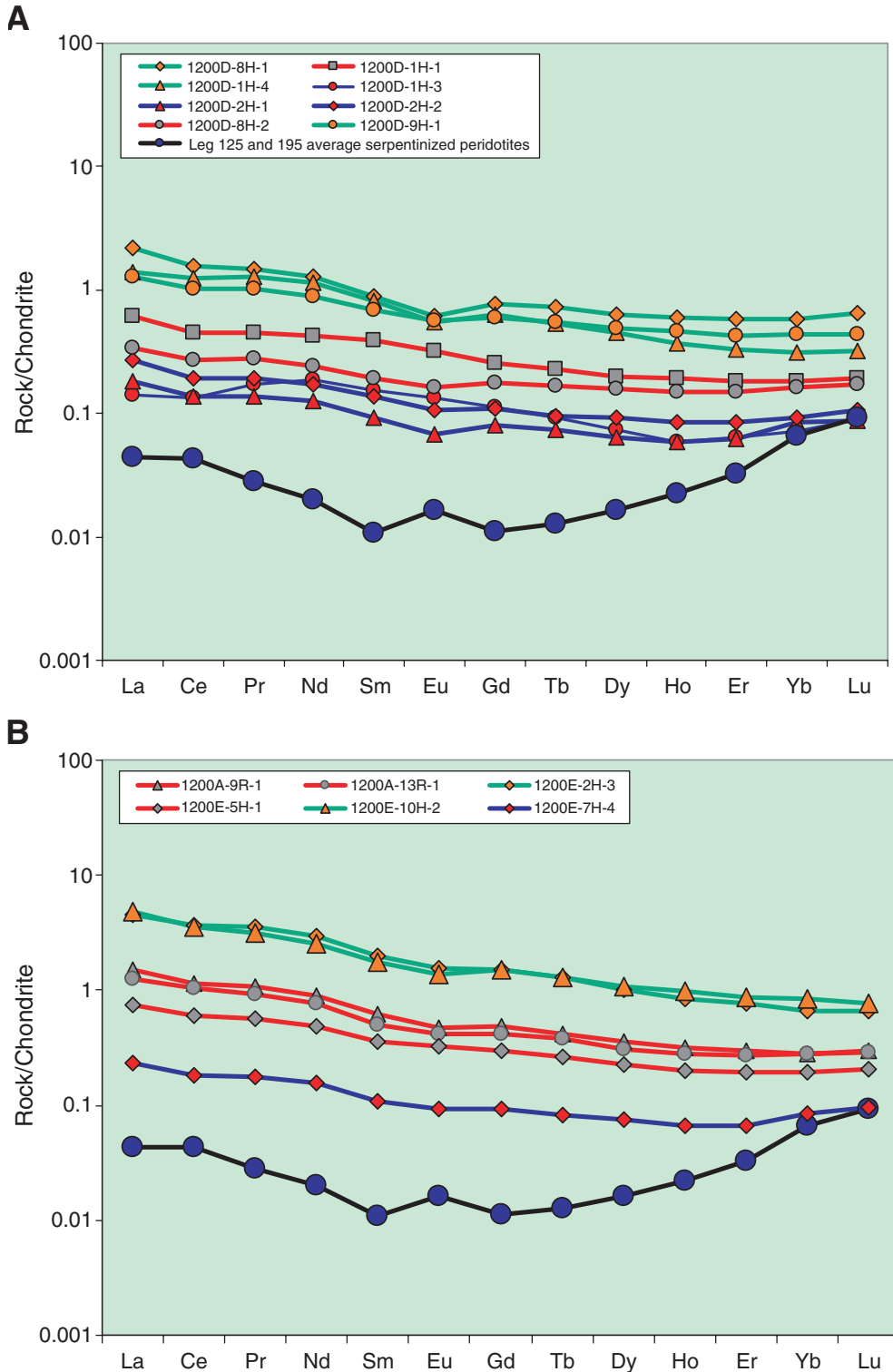


Figure F9. A. MgO vs. SiO₂ for serpentinite muds and metamorphic clasts from Legs 125 and 195. The shaded field is for serpentinitized peridotites (Savov, 2004). Note how the metamorphic rocks with ultramafic protolith overlap the field with the Leg 195 serpentinite muds and how the metabasic clasts with MORB-like protolith have low MgO. **B.** SiO₂ vs. CaO for serpentinite muds and metamorphic clasts from ODP Legs 125 and 195. The shaded field is for serpentinitized peridotites (Savov, 2004). Note the similarity of the Leg 195 metamorphic schists and the metabasalts recovered from Leg 125 (Johnson, 1992). The metamorphic schists also show consistently high CaO (>3 wt%). (Continued on next page.)

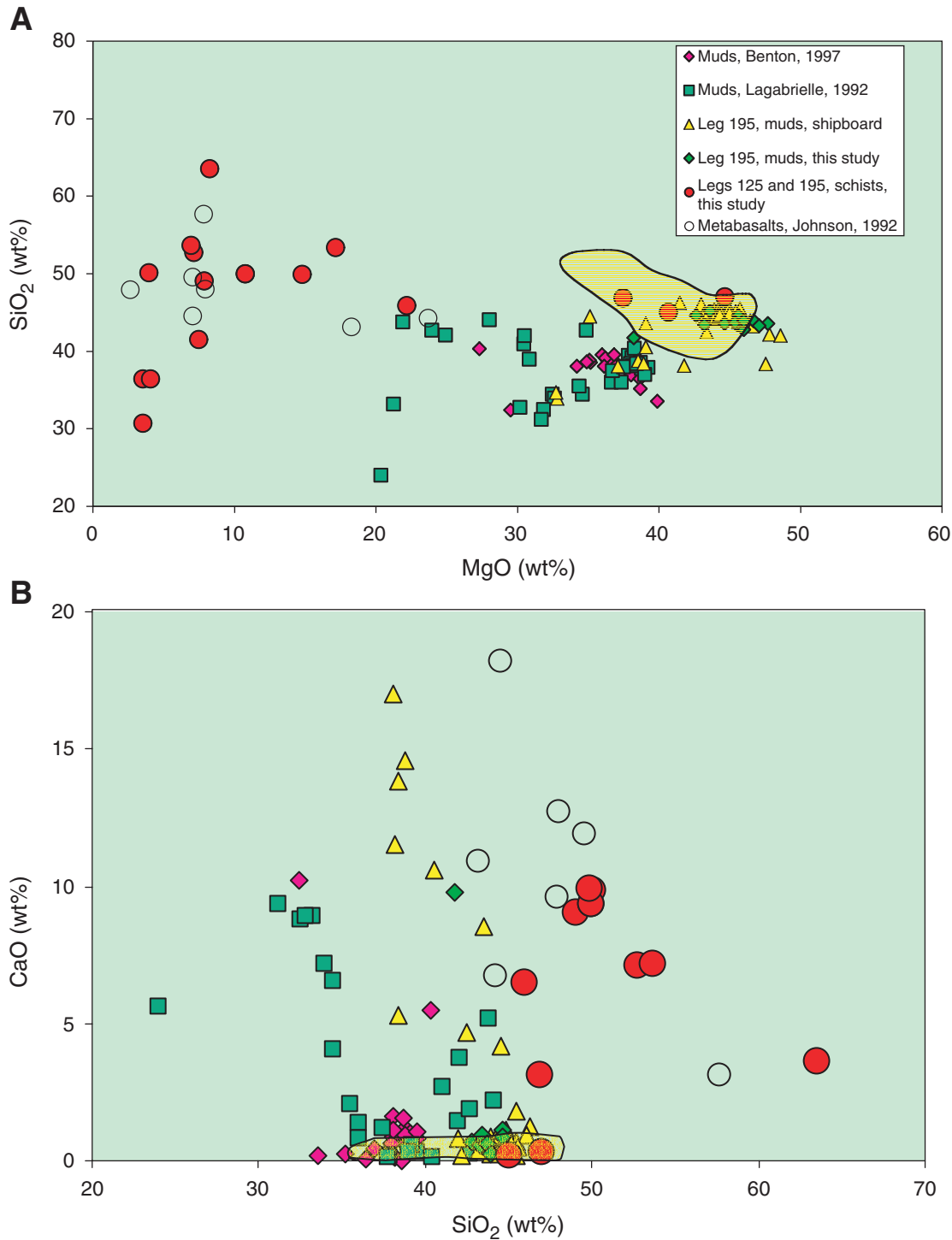


Figure F10. A. Al_2O_3 vs. SiO_2/MgO for serpentinite muds and metamorphic clasts from Legs 125 and 195. There exists a clear distinction between the serpentinite muds and the metamorphic schists with ultramafic protoliths (with $\text{Al}_2\text{O}_3 < 3$ wt% and $\text{Si}/\text{Mg} \sim 1$), and the schists with MORB-like protoliths (with $\text{Al}_2\text{O}_3 > 3$ wt% and $\text{Si}/\text{Mg} > 1$). There is also a positive correlation between the Al_2O_3 and Si/Mg ratio for the Leg 125 metabasalts (Johnson, 1992) and the MORB-like schists from Leg 195. The shaded field is for serpentinitized peridotites (Savov, 2004). **B.** CaO vs. SiO_2/MgO for serpentinite muds and metamorphic clasts from Legs 125 and 195. The serpentinite muds are clearly different from the metamorphic schists in that they have low Si/Mg (~ 1). The MORB samples from Leg 125 (Johnson, 1992) and the metabasic schists from Leg 195 have $\text{Ca} > 3$ wt% and $\text{Si}/\text{Mg} > 1$. (Continued on next page.)

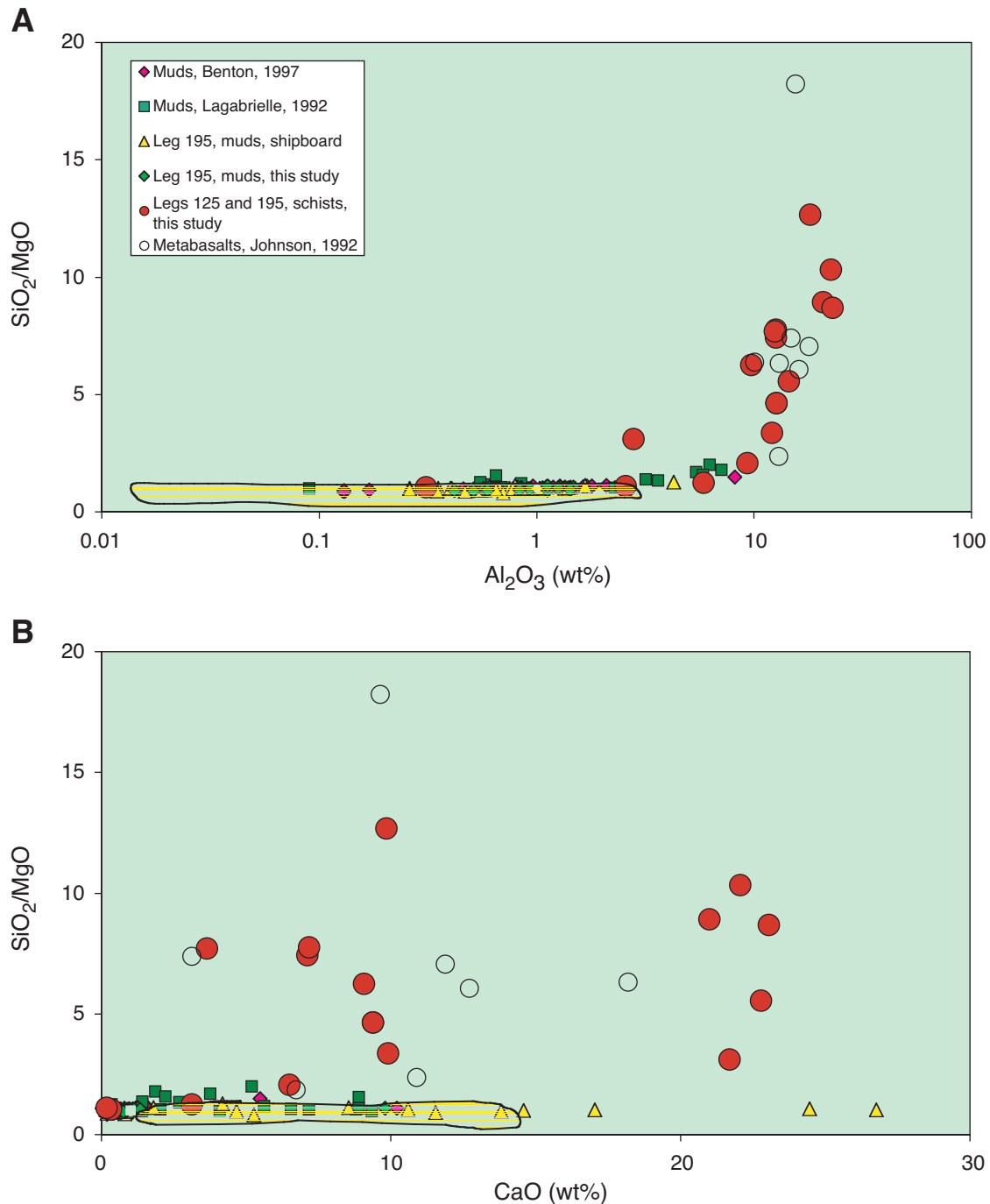


Figure F10 (continued). C. TiO_2 vs. SiO_2/MgO for serpentinite muds and metamorphic clasts from Legs 125 and 195. As in Figure F5A, p. 20, the schists with basaltic protolith have high TiO_2 (1 wt%) and $\text{Si}/\text{Mg} > 1$. They also show positive TiO_2 - SiO_2/MgO correlation. Note that the scale for TiO_2 is logarithmic. Symbols are the same as in A.

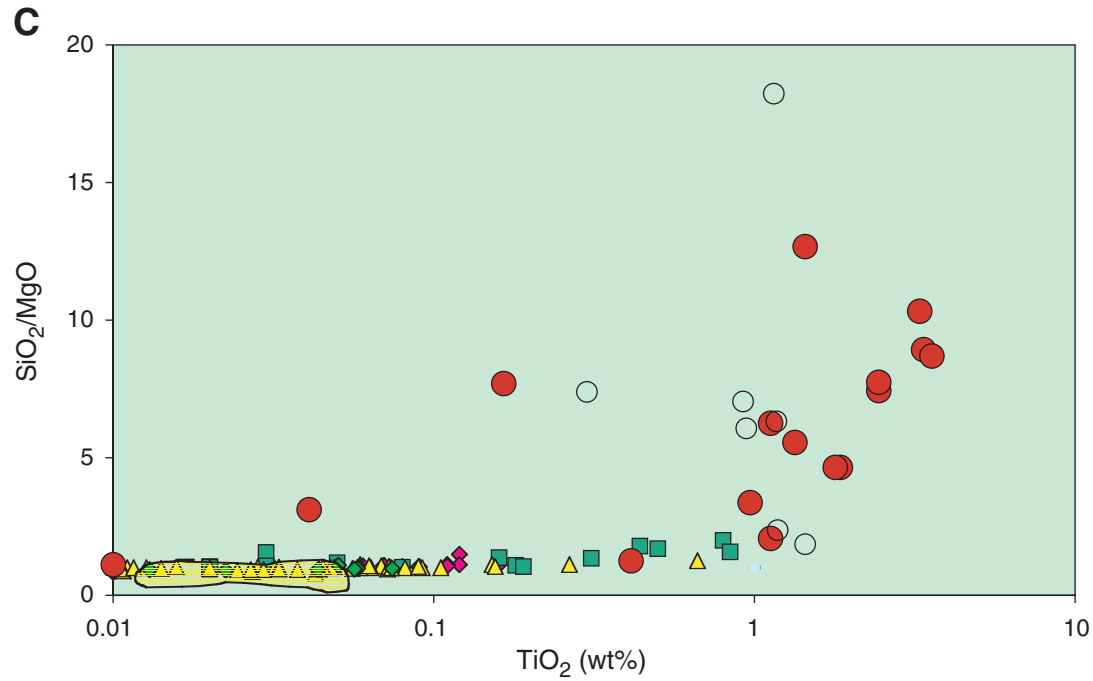


Figure F11. A. Li vs. SiO_2/MgO for serpentinite muds and metamorphic clasts from Legs 125 and 195. Lithium is elevated in most of the metamorphic clasts in respect to the muds. The Li abundances of Leg 195 and Leg 125 (Benton, 1997) serpentinite muds are similar. Lithium shows positive correlation with SiO_2/MgO only in the metabasic samples with MORB-like protoliths. Depleted mantle Li = ~1.6 ppm (Ryan and Langmuir, 1987). The shaded field is for serpentinitized peridotites (Savov, 2004). B. B vs. SiO_2/MgO for serpentinite muds and metamorphic clasts from Legs 125 and 195. The high B content of all of the metamorphic schists remains independent of their protolith (discriminated by SiO_2/MgO ratio as in Fig. F10, p. 28) and resemble the B contents of serpentinite muds. The B abundances of serpentinite muds from ODP Legs 195 (this study) and 125 (Benton, 1997) are similar.

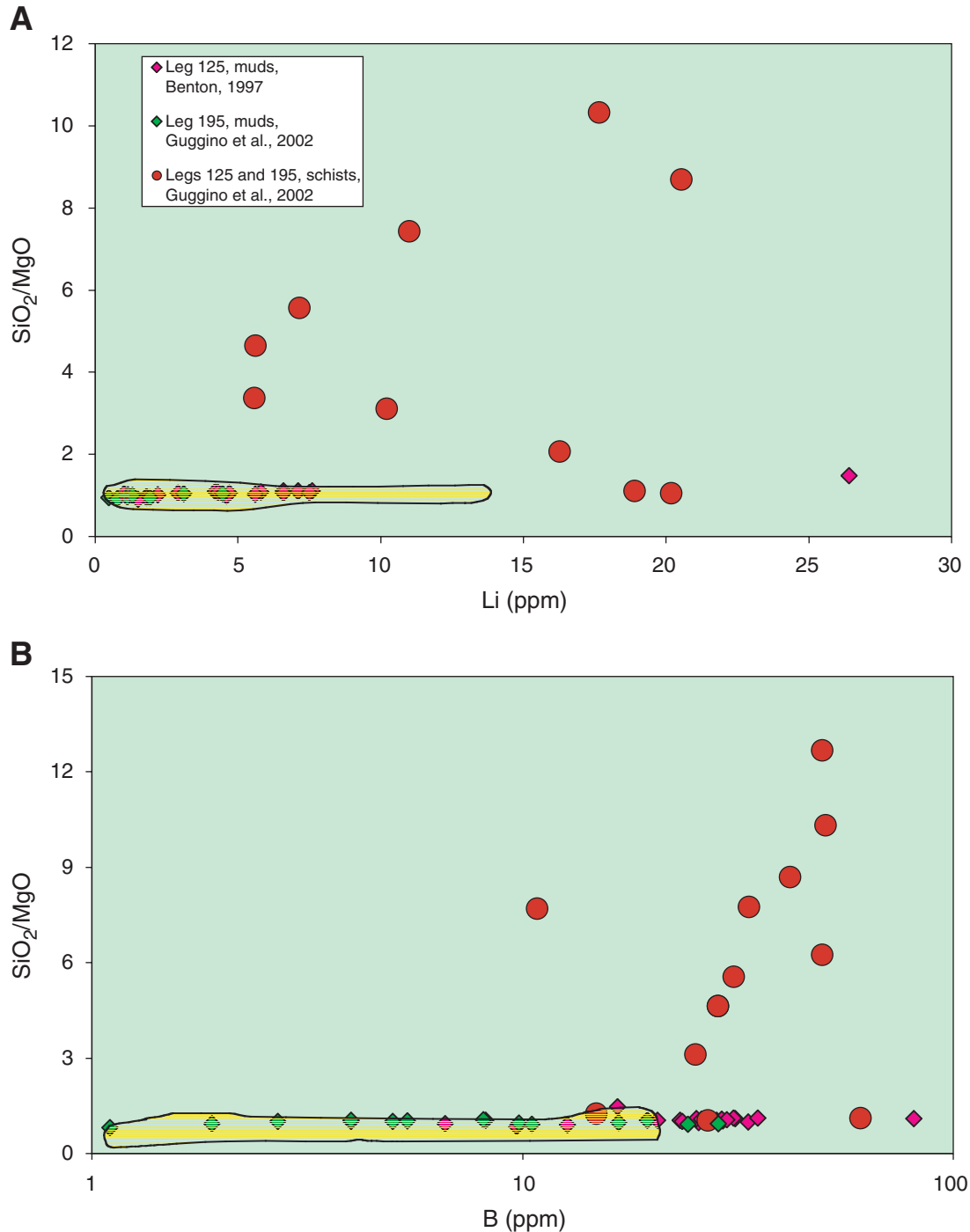


Figure F12. TiO_2 vs. B for serpentinite muds and metamorphic clasts from Legs 125 and 195. Depleted mantle B = ~0.25 ppm (Ryan and Langmuir, 1993). The B enrichments in the metamorphic clasts are independent of their protolith type (expressed as variable TiO_2).

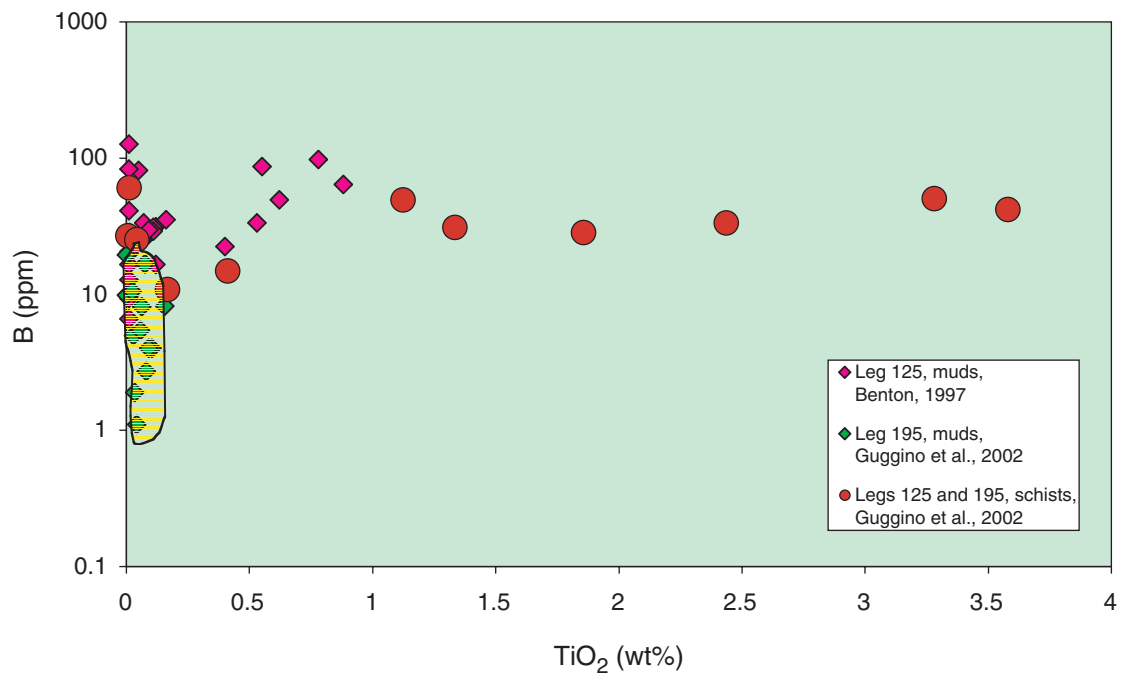


Figure F13. Depleted mantle normalized plot of fluid-mobile elements from the metamorphic clasts and serpentinite muds from ODP Legs 125 and 195. In the mud data we used only the deep core samples in order to minimize the effect of seawater. Depleted mantle values are from Salters and Stracke (2004). avg. = average.

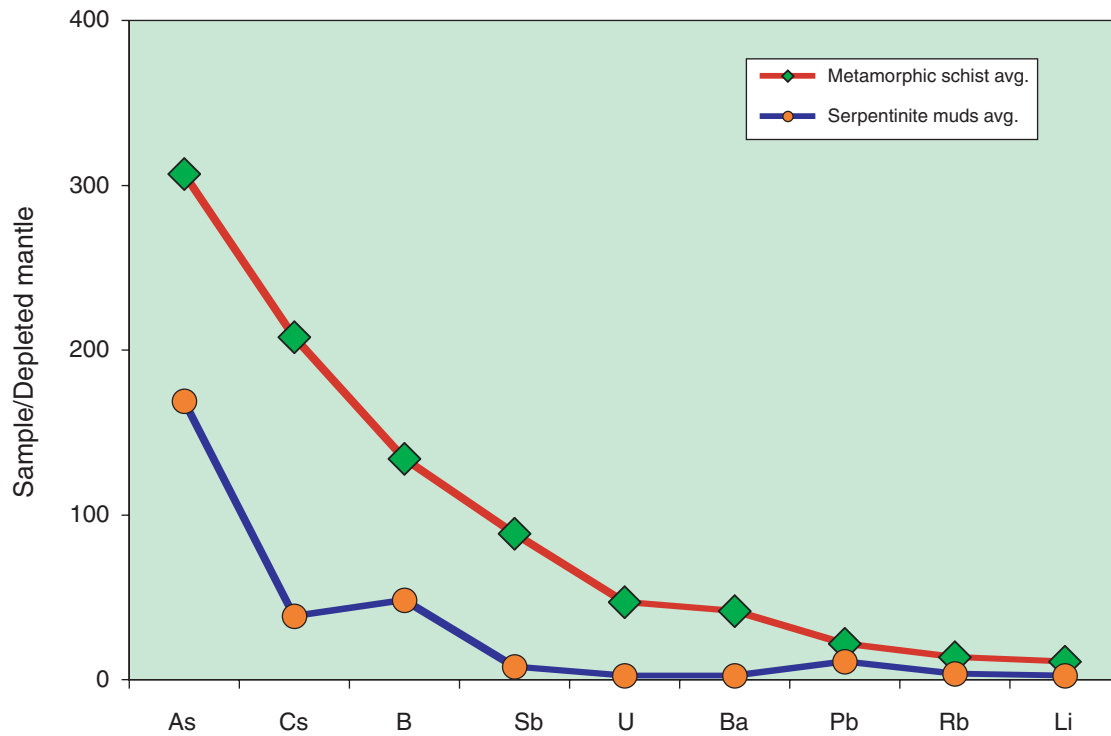


Figure F14. Coryell-Masuda diagram for metamorphic clasts from Legs 125 and 195, normalized to chondrites (Nakamura, 1974). Note that Sample 195-1200D-8H, 119–121 cm, shows a different REE (especially LREE) pattern and is very LREE enriched. Such REE abundance levels resemble those of evolved island arc lavas or sediments. The REE pattern of this sample also resembles the slightly enriched LREE patterns of the serpentinite muds (Fig. F8, p. 25). The REE abundances and patterns for the rest of the metamorphic clasts resemble those of altered oceanic crust from mid-ocean-ridge settings (Kelley et al., 2003).

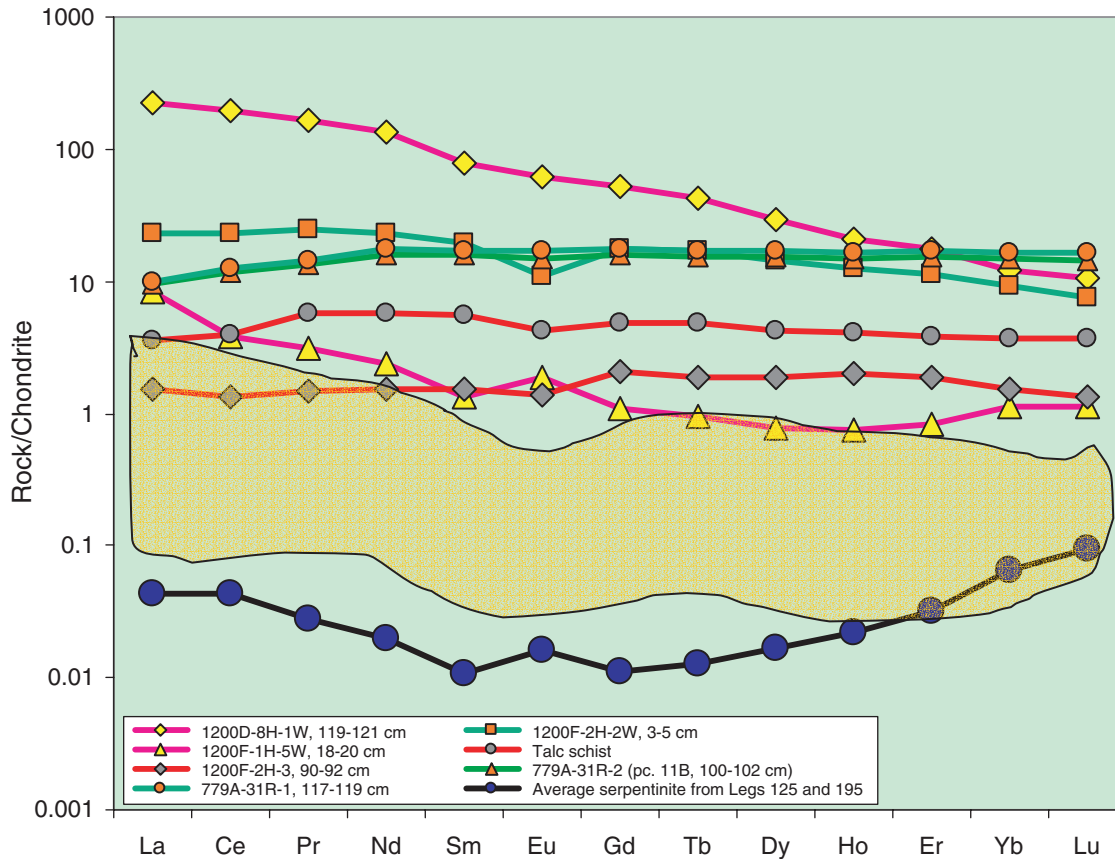


Figure F15. Plots showing mixing curves between the average serpentinized peridotites and average metamorphic clasts (see data in Table T8, p. 48). All samples considered are from core depths of >10 mbsf. The plots show that the serpentinite muds contain up to 5% of metamorphic clast material. A. Yb vs. Th. B. Yb vs. Nd. (Continued on next two pages.)

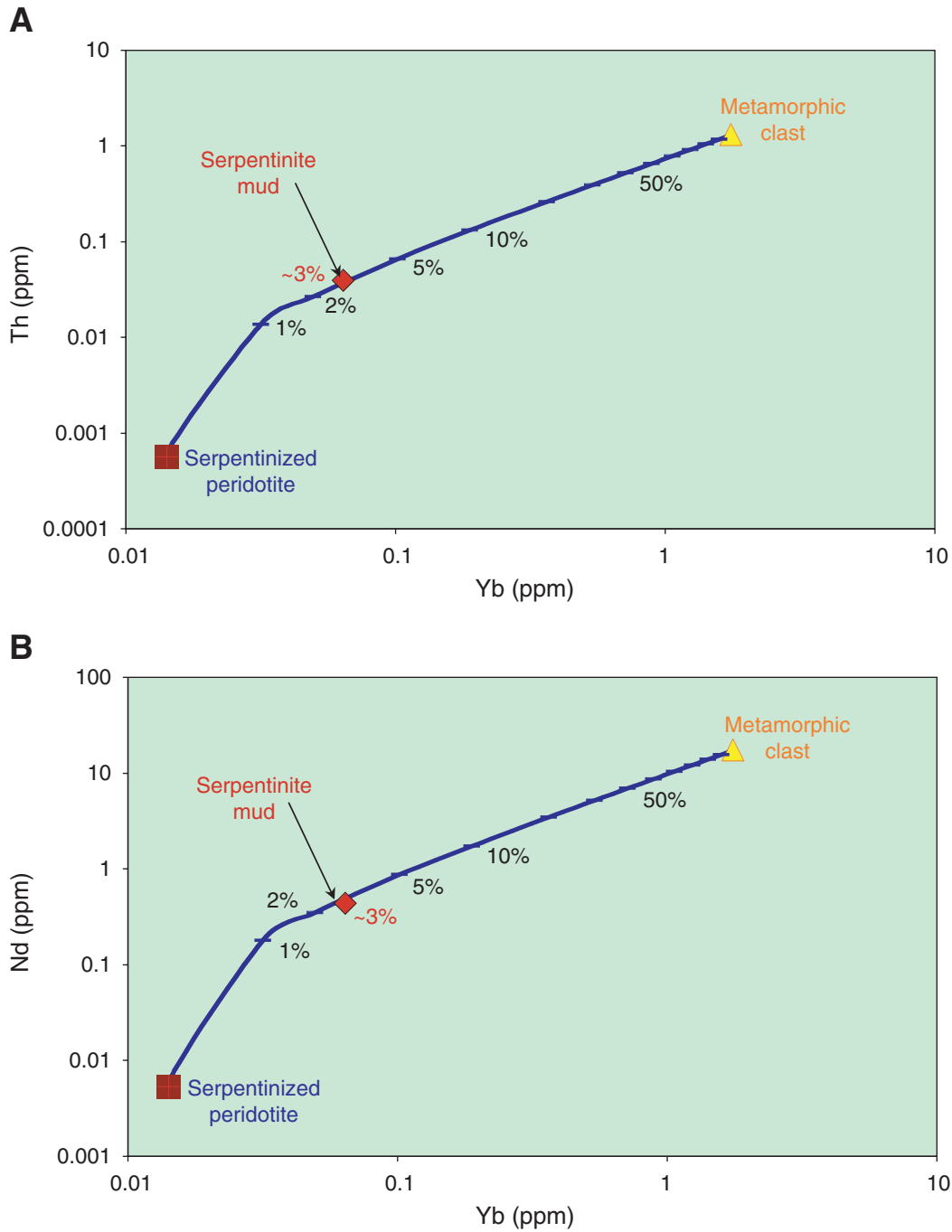


Figure F15 (continued). C. Yb vs. Sc. D. Al₂O₃ vs. Ba/Yb.

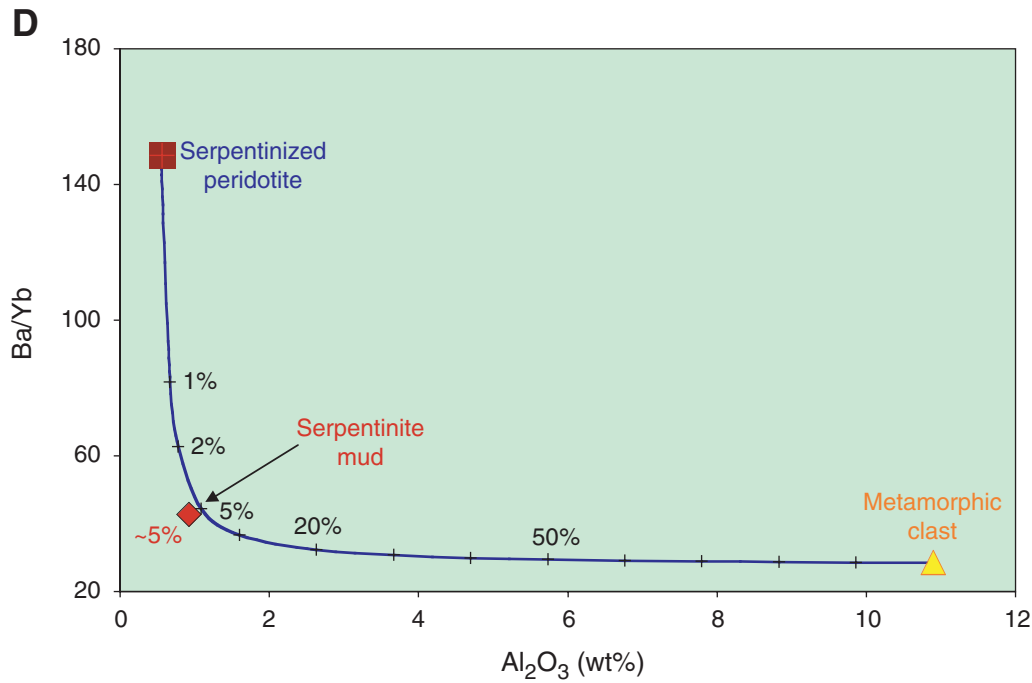
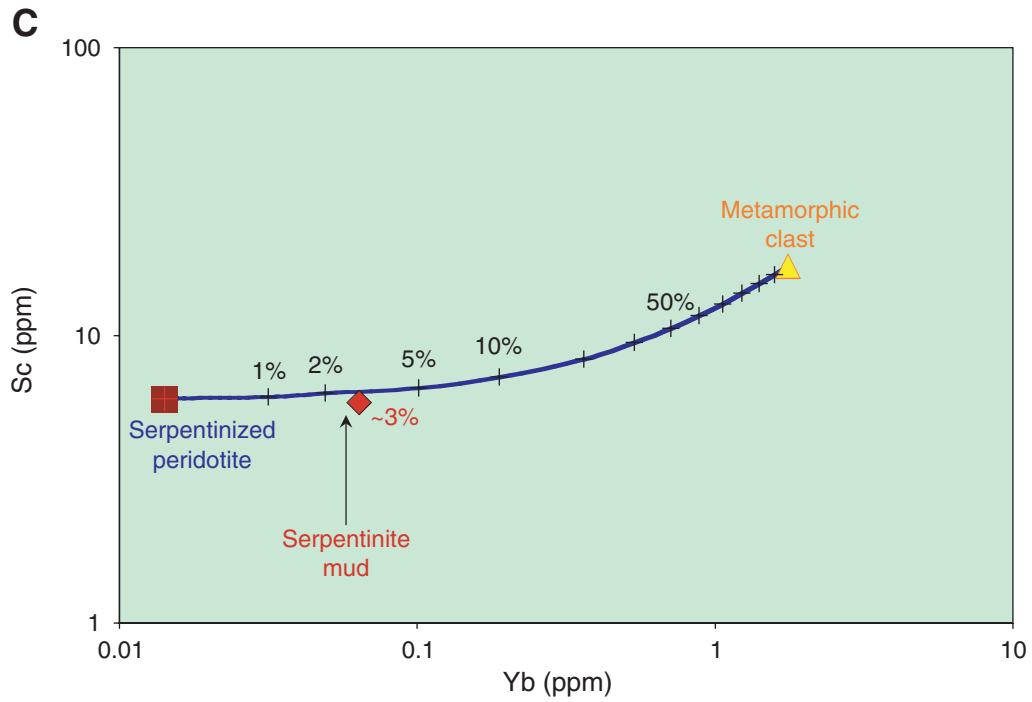


Figure F15 (continued). E. Al_2O_3 vs. Rb/Yb.

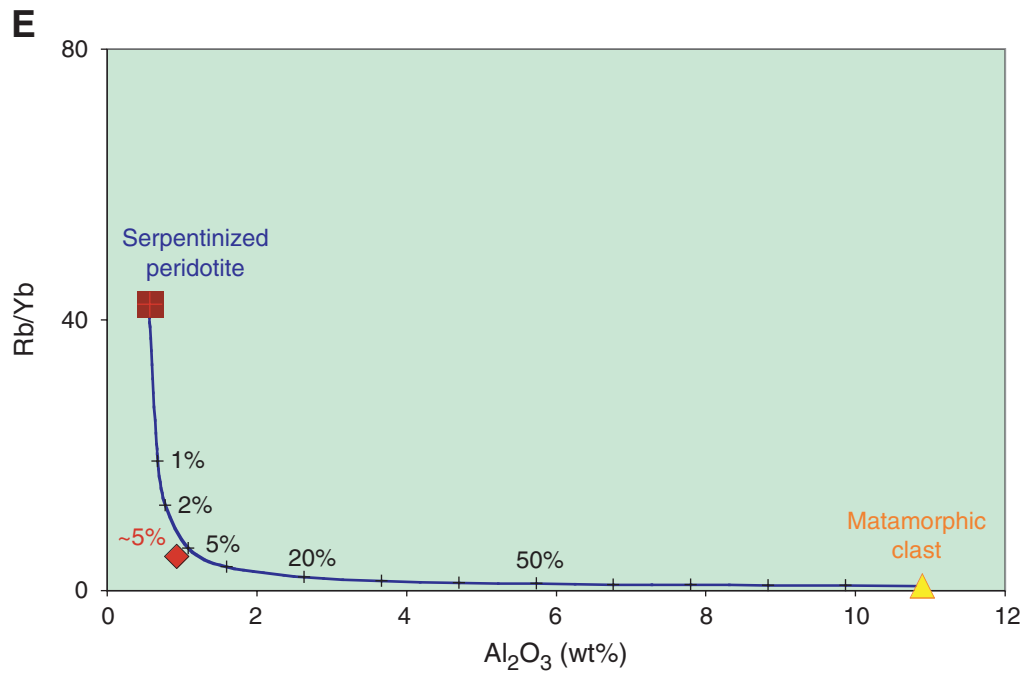


Table T1. Shipboard ICP-AES major and trace elements analysis of serpentinite muds. (Continued on next three pages.)

Core, section interval (cm):	195-1200A				195-1200E									
	9R-1 63-65	1H-1 50-52	1H-2 100-102	1H-2 70-72	2H-1 128-130	2H-2 126-128	2H-3 120-122	4H-3 115-117	5H-3 47-49	7H-2 127-129	7H-4 124-126	10H-1 113-115	10H-2 62-64	10H-2 127-129
Depth (mbsf):	71.03	0.50	1.00	2.20	7.38	8.86	10.30	16.15	20.58	28.67	31.64	53.53	54.52	55.17
Major element oxide (wt%):														
SiO ₂	43.90	33.90	38.17	44.45	45.42	45.42	46.25	42.48	44.33	44.21	44.91	44.50	44.92	44.88
TiO ₂	0.07	0.02	0.02	0.03	0.26	0.05	0.15	0.01	0.07	0.09	0.06	0.66	0.01	0.16
Al ₂ O ₃	0.95	0.33	0.48	0.63	2.45	0.85	1.68	0.34	0.86	1.04	0.75	4.27	0.40	1.43
Fe ₂ O ₃ T	8.40	5.61	6.96	8.12	8.37	8.12	8.22	8.25	8.45	8.84	8.26	9.52	8.67	8.27
MnO	0.12	0.09	0.10	0.13	0.14	0.12	0.13	0.11	0.14	0.15	0.14	0.16	0.14	0.15
MgO	45.95	32.81	41.77	44.87	40.62	43.90	41.46	43.35	44.29	44.00	44.41	35.12	45.01	43.18
CaO	0.88	26.76	11.54	0.78	1.80	0.66	1.26	4.67	0.88	0.83	0.67	4.18	0.65	1.11
Na ₂ O	0.96	0.47	0.91	0.93	0.85	0.83	0.76	0.67	0.93	0.80	0.76	1.31	0.18	0.76
K ₂ O	0.15	0.01	0.04	0.06	0.08	0.06	0.08	0.13	0.04	0.03	0.02	0.20	0.01	0.03
P ₂ O ₅	0.03	0.01	0.00	0.00	0.02	0.00	0.02	0.01	0.02	0.03	0.02	0.07	0.01	0.03
Totals:	101.38	100.00	100.00	100.00	100.00	100.00	100.00	100.00	100.00	100.00	100.00	100.00	100.00	100.00
LOI	15.22	22.50	19.93	15.42	12.94	13.91	13.49	17.00	14.67	13.94	8.77	12.08	16.42	13.83
Trace element (ppm):														
Sc	6.5	4.7	6.2	7.1	10.9	9.1	8.0	6.8	6.8	6.9	6.4	10.7	6.3	7.6
V	28.4	18.2	20.2	22.9	57.8	29.9	33.8	15.9	22.2	22.8	23.6	66.4	13.6	28.6
Cr	2342	1617	2316	2334	2118	2363	2212	1944	3311	2595	2788	2410	1856	2743
Ni	2428	4345	2284	2800	3184	2475	2241	2771	2905	2841	2871	2274	3490	2718
Sr	23.5	4821	1567	44.7	21.1	13.0	21.1	639	13.4	12.0	11.6	39.2	35.9	15.7
Ba	4.9	18.0	21.6	7.8	14.2	5.7	12.8	6.8	15.1	7.4	6.6	37.5	6.1	8.7
Zr	8.2	2.6	0.0	6.7	24.4	10.4	16.8	2.7	10.3	7.3	5.9	49.8	1.7	13.8
Y	2.6	2.1	0.6	0.7	6.0	3.1	3.4	0.1	0.7	0.8	0.4	4.4	0.1	2.7
B (DCP-AES)														8.2
Li (DCP-AES)		1.6	0.9	1.4	7.6	4.9	5.2	0.7	1.8	2.8	1.8	9.8	0.6	4

Note: DCP-AES = direct-current plasma-atomic emission spectrometer, LOI = loss on ignition.

Table T1 (continued).

Core, section interval (cm):	195-1200E					
	4H-1 128-130	4H-2 128-130	5H-1 79-81	5H-2 78-80	6H-1 119-121	6H-3 117-119
Depth (mbsf):	13.28	14.78	18.39	19.83	22.39	25.31
Major element (wt%):						
SiO ₂	38.39	40.54	43.77	44.73	43.48	43.23
TiO ₂	0.06	0.07	0.04	0.07	0.03	0.03
Al ₂ O ₃	0.77	1.07	0.65	0.84	0.55	0.54
Fe ₂ O ₃ T	6.88	7.52	8.36	8.31	8.16	8.28
MnO	0.09	0.13	0.13	0.13	0.12	0.13
MgO	38.92	39.07	45.60	44.28	46.24	46.63
CaO	13.81	10.59	0.56	0.66	0.43	0.37
Na ₂ O	0.90	0.83	0.76	0.83	0.80	0.67
K ₂ O	0.08	0.10	0.07	0.07	0.08	0.06
P ₂ O ₅	0.10	0.08	0.07	0.07	0.10	0.07
Totals:	100.00	100.00	100.00	100.00	100.00	100.00
LOI	18.95	17.44	15.70	14.44	15.24	14.96
Trace element (ppm):						
Sc	6.7	7.5	7.8	7.7	7.2	8.2
V	30.9	28.7	23.7	24.3	19.7	23.3
Cr	2066	2136	2214	2330	2420	2518
Ni	1942	2226	5272	-	-	5619
Sr	2007	1358	24.9	14.8	16.9	18.6
Ba	44.3	25.6	22.3	13.8	10.9	9.6
Zr	10.4	10.7	9.1	8.2	9.6	11.9
Y	2.3	3.2	1.4	1.5	1.6	0.7
B (DCP-AES)						
Li (DCP-AES)	7.6	3.4	1.4	2	1.5	2.5

Table T1 (continued).

Core, section interval (cm):	19S-1200D														
	2H-2 40-42	3H-1 52-54	5H-1 17-19	6H-1 96-98	7H-1 103-105	8H-2 95-97	9H-1 64-66	1H-1 0-2	1H-1 50-52	1H-1 100-102	1H-CC 32-34	1H-2 70-72	1H-3 38-40	1H-4 62-64	2H-1 60-62
Depth (mbsf):	8.80	10.42	13.87	22.46	24.53	27.45	28.64	0.00	0.50	1.00	6.72	2.20	3.38	5.12	7.50
Major element oxide (wt%):															
SiO ₂	44.85	45.47	45.11	45.41	46.08	45.54	45.19	43.56	38.05	38.81	42.19	43.41	42.01	43.94	44.42
TiO ₂	0.05	0.01	0.01	0.05	0.07	0.03	0.06	0.06	0.03	0.02	0.01	0.04	0.03	0.01	0.06
Al ₂ O ₃	0.84	0.26	0.35	0.81	1.14	0.57	0.85	0.80	0.67	0.41	0.35	0.58	0.47	0.26	0.91
Fe ₂ O ₃ T	7.98	7.54	7.95	8.11	7.89	7.68	8.29	7.17	6.36	6.87	9.15	7.72	7.21	8.16	8.16
MnO	0.12	0.11	0.12	0.12	0.13	0.11	0.13	0.07	0.08	0.10	0.15	0.11	0.11	0.12	0.13
MgO	44.65	45.72	45.41	44.19	42.97	44.96	44.30	39.09	37.11	38.54	47.82	46.45	48.60	46.47	44.86
CaO	0.67	0.21	0.22	0.66	0.96	0.51	0.55	8.53	17.04	14.59	0.19	0.84	0.81	0.28	0.67
Na ₂ O	0.79	0.63	0.78	0.61	0.72	0.55	0.59	0.70	0.64	0.65	0.13	0.81	0.74	0.72	0.75
K ₂ O	0.05	0.03	0.04	0.04	0.05	0.04	0.04	0.01	0.02	0.02	0.01	0.03	0.03	0.03	0.03
P ₂ O ₅	0.00	0.00	0.00	0.02	0.00	0.00	0.02	0.02	0.00	0.00	0.02	0.00	0.00	0.00	0.00
Totals:	100.00	100.00	100.00	100.00	100.00	100.00	100.00	100.00	100.00	100.00	100.00	100.00	100.00	100.00	100.00
LOI	15.67	15.08	15.29	12.02	14.20	14.35	14.76	18.23	22.50	19.60	16.07	15.42	16.95	15.83	14.86
Trace element (ppm):															
Sc	9.2	5.5	6.8	8.3	8.1	6.1	7.5	7.1	6.0	5.3	9.6	6.8	5.9	5.8	7.6
V	27.1	16.1	17.7	22.0	29.9	20.8	27.2	32.9	25.1	19.6	22.3	22.7	17.4	19.6	28.7
Cr	2340	2269	2976	2002	2538	2552	2781	2228	1967	2208	2742	2063	2004	2183	2570
Ni	2467	2328	4074	2615	2494	2883	2999	1502	1902	2107	3836	4014	2420	2801	2509
Sr	12.9	5.7	7.7	14.6	19.7	10.5	13.9	1548	2961	1958	15.0	30.9	11.4	5.7	8.8
Ba	5.7	6.4	1.8	2.3	2.7	1.8	8.0	12.8	15.2	14.0	5.1	6.3	6.2	4.5	14.2
Zr	10.1	9.3	8.0	13.1	2.8	11.5	10.7	2.8	2.3	1.0	2.3	5.7	3.9	3.9	8.1
Y	2.8	2.0	1.4	1.6	2.5	0.7	2.6	2.6	2.1	20.8	1.2	2.0	1.2	1.8	2.8
B (DCP-AES)						5	5.4								
Li (DCP-AES)	0.9	1.4	0.8	2.3	2.8	1.1	2.6	2.4	2.1	1.3		1.5	1.4	0.4	2.6

Table T1 (continued).

Core, section interval (cm):	195-1200F					
	1H-1 10-12	1H-1 86-88	1H-2 55-57	1H-2 133-136	2H-2 135-137	2H-4 66-68
Depth (mbsf):	0.10	0.86	2.05	2.86	10.55	12.36
Major element oxide (wt%):						
SiO ₂	34.67	38.38	44.43	43.48	44.53	45.14
TiO ₂	0.06	0.04	0.08	0.03	0.11	0.09
Al ₂ O ₃	0.82	0.70	1.07	0.62	1.35	1.40
Fe ₂ O ₃ T	6.39	7.06	8.33	7.88	7.68	8.06
MnO	0.10	0.12	0.15	0.12	0.13	0.13
MgO	32.71	47.53	43.99	45.99	44.23	43.56
CaO	24.46	5.27	0.85	0.83	0.96	0.61
Na ₂ O	0.72	0.80	1.05	0.96	0.85	0.84
K ₂ O	0.02	0.02	0.04	0.08	0.09	0.10
P ₂ O ₅	0.05	0.08	0.02	0.01	0.08	0.07
Totals:	100.00	100.00	100.00	100.00	100.00	100.00
LOI	21.95	7.24	15.86	16.07	14.40	14.60
Trace element (ppm):						
Sc	5.4	5.4	7.2	7.2	8.8	9.4
V	35.3	20.5	24.6	21.8	31.4	29.9
Cr	2544	2407	3098	2799	2140	2305
Ni	1748	2335	3215	2742	2443	2603
Sr	2976	438	13.9	21.7	21.5	22.5
Ba	29.5	27.6	9.1	14.4	18.6	19.5
Zr	9.2	6.7	10.1	8.0	10.5	7.8
Y	1.8	0.7	0.9	1.1	4.7	2.7
B (DCP-AES)	8.1	1.1	2.7	1.9	4	4
Li (DCP-AES)						

Table T2. Shore-based major and trace elements analysis of serpentinite muds. (Continued on next page.)

Core, section interval (cm):	195-1200A				195-1200B			195-1200D							
	9R-1 77-79	9R-1 27-29	9R-1 63-65	13R-1 1-3	2H-1 52-54	1H-1 15-17	2H-1 124-126	2H-2 81-83	1H-2 118-120	8H-1 119-121	1H-2 100-102	5H-1 6-9	1H-1 54-56	8H-1 127-129	1H-3 116-118
Depth (mbsf):	71.17	70.67	71.03	108.71	31.22	0.15	8.14	9.21	2.68	26.19	2.50	13.76	0.54	26.27	4.16
Major element oxide (wt%):															
SiO ₂		43.42	44.82	43.75	42.91	41.73	43.94	43.61	43.30	35.76	43.30	42.94	45.15		43.90
TiO ₂	0.08	0.00	0.04	0.06	0.01	0.05	0.01	0.02	0.04	3.92	0.01	0.01	0.01		0.00
Al ₂ O ₃		1.15	0.79	0.72	0.78	1.12	0.60	0.42	0.51	21.16	0.38	0.77	1.04		1.43
Fe ₂ O ₃ T		8.66	8.01	8.35	8.18	6.77	8.12	8.64	8.07	13.21	7.93	8.81	8.19		8.14
MnO		0.13	0.11	0.12	0.12	0.07	0.11	0.12	0.11	0.18	0.10	0.14	0.10		0.12
MgO		43.22	44.54	45.39	47.31	38.23	46.68	47.71	47.09	3.04	45.66	45.38	43.04		46.01
CaO		0.94	0.46	0.65	0.58	9.80	0.34	0.68	0.57	21.33	0.12	0.30	0.45		0.24
Na ₂ O		0.15	0.08	0.05	0.09	0.11	0.04	0.04	0.06	0.28	0.08	0.16	0.40		0.03
K ₂ O	0.03	0.07	0.04	0.03	0.02	0.05	0.02	0.02	0.06	0.03	0.03	0.04	0.04	0.03	0.05
P ₂ O ₅															
Totals:		97.74	98.92	99.14	100.01	97.94	99.87	101.25	99.77	95.00	97.62	98.52	98.42		99.90
LOI	16.30	14.57	14.20	15.00	14.20	16.45	15.09	13.00	17.20	7.60	14.60	18.70	21.20	15.10	15.98
Trace element (ppm):															
Sc	10.8	12.1	22.6	15.4	8.4	11.2	16.6	10.9	12.6	43.1	16.8	19.8	19.7	12.2	6.4
V	38.2	46.7	85.4	58.0	18.6	43.7	72.0	44.1	53.1	216.0	56.6	73.6	64.8	44.9	16.7
Cr		3263	2011	2929	2210	2950	3114	2507	2243	54	2461	2973	3748		2382
Ni	3652	5377	4738	5584	3377	2648	4145	4537	6162	130	4737	4486	5297	3492	5240
Sr		14.3	10.5	19.8	15.3	1756.6	6.9	59.6	52.6	321.5	3.5	15.2	71.3		4.7
Ba	4.4	30.0	13.0	5.1	3.3	10.6	5.2	3.6	5.7	317.4	8.6	10.1	8.8	4.0	0.8
Zr	12.3	13.3	19.4	13.4	6.2	13.3	14.2	12.1	13.9	23.4	15.2	14.0	19.1	10.6	7.7
Y	98.3	185.5	61.1	64.4	59.9	72.3	63.4	57.9	60.3	127.2	60.3	72.4	65.6	51.7	57.5
B (DCP-AES)			19.2	13.2			28.5	10.5	24.2						
Li (DCP-AES)	2.4	3.4	2.4	1.3										21.1	

Notes: Boron and Li concentrations were analyzed on the direct-current plasma-atomic emission spectrometer at USF. LOI = loss on ignition.

Table T2 (continued).

Core, section interval (cm):	195-1200E				195-1200F		
	2H-3 34-36	5H-1 40-42	5H-2 84-86	5H-1 37-39	1H-4 6-8	2H-2 3-5	1H-5 18-20
Depth (mbsf):	9.44	18.00	19.89	17.97	4.56	9.23	6.18
Major element oxide (wt%):							
SiO ₂	44.66	43.43	43.55	42.78	44.67	45.18	43.50
TiO ₂	0.00	0.00	0.07	0.00	0.06	0.00	0.06
Al ₂ O ₃	1.47	0.57	0.84	1.12	0.93	1.26	0.83
Fe ₂ O ₃ T	8.30	8.27	8.23	8.21	8.11	7.73	8.08
MnO	0.12	0.12	0.12	0.12	0.12	0.11	0.12
MgO	42.64	45.61	44.65	45.98	45.62	43.58	45.50
CaO	1.13	0.60	0.66	0.68	0.85	1.33	0.75
Na ₂ O	0.14	0.03	0.05	0.06	0.15	0.16	0.11
K ₂ O	0.03	0.05	0.03	0.03	0.03	0.03	0.04
P ₂ O ₅							
Totals:	98.56	98.67	98.20	99.01	100.58	99.43	98.98
LOI	14.22	16.94	16.77	16.00	15.50	14.30	14.90
Trace element (ppm):							
Sc	7.7	12.2	14.1	20.0	17.2	11.2	1.7
V	25.9	47.0	52.6	80.9	62.6	37.2	3.2
Cr	2344	2698	2639	2874	1942	1966	2274
Ni	4399	5443	5000	5332	3527	3052	3504
Sr	20.2	12.4	15.3	9.4	30.0	9.5	12.5
Ba	13.9	10.7	11.4	13.9	14.2	7.4	11.6
Zr	11.2	12.5	14.7	16.8	20.6	13.3	6.2
Y	55.9	526	62.2	199	56.5	53.7	49.9
B (DCP-AES)	19.5	9.8	16.7				
Li (DCP-AES)							

Table T3. Shore-based ICP-MS analysis of serpentinite muds from Leg 125 and 195.

Core, section interval (cm):	195-1200A		195-1200D						195-1200E			195-1200D*		195-1200E*
	9R-1 63–65	13R-1 1–3	2H-1 124–126	2H-2 81–83	8H-1 127–129	1H-1 116–118	1H-4 115–117	1H-3 116–118	2H-3 34–36	5H-1 40–42	7H-4 127–129	8H-2 95–97	9H-1 64–66	10H-2 127–129
Depth (mbsf):	71.03	108.71	8.14	9.21	26.24	1.16	5.65	4.16	9.44	18.00	31.67	27.45	28.64	55.17
TiO ₂ (wt%)	0.036		0.006	0.009	0.036	0.070	0.031	0.009						
Trace element (ppm):														
B (DCP-AES)	19.2	13.2	28.5	10.5	15.0	13.0	22.1	15.4	19.5	9.8	10.6	5.0	5.4	8.2
Li (DCP-AES)	2.4	1.3										1.1	2.6	4
Li	1.3	1.1	0.5	0.8	1.6	0.7	1.0	0.3	3.1	1.9	0.7	1.1	2.8	4.5
Be	0.02	0.04	0.004	0.01	0.08	0.02	0.03	0.01	0.08	0.01	0.004	0.01	0.03	0.06
Sc	6.4	6.3	5.0	5.7	6.6	3.8	6.1	6.0	6.7	5.6	5.5	5.4	6.3	7.1
V	7.9			1.4	14.6		4.3	0.5						
Cr	2954		1943	2239	2418	1589	2523	2176						
Co	112		106	114	103	71	108	111						
Ni	2287		2088	2150	1938	1354	2084	2136						
Cu	8.6	4.5	3.1	3.2	3.4	4.0	5.5	3.5	7.7	4.4	2.7			
Zn	15.0		10.1	11.5	11.6	10.3	11.4	10.6						
Ga	0.7	0.6	0.3	0.3	0.9	0.3	0.6	0.2	1.5	0.5	0.3			
As	1.2	0.8	2.0	1.6	1.9	0.9	1.5	1.7	0.9	0.7	0.7	2.24	0.87	0.84
Rb	0.4	0.4	0.1	0.1	0.3	0.5	0.1	0.0	1.0	0.2	0.1	0.5	0.6	0.8
Sr	8.98	8.39	2.30	29.53	10.00	1839	4.41	2.39	17.09	9.20	8.80			
Y	0.6	0.5	0.1	0.2	1.3	0.5	0.8	0.1	1.7	0.4	0.1	0.3	1.0	2.0
Zr	2.1	2.9	0.4	0.5	1.5	1.6	2.1	0.2	8.1	1.5	0.5	0.9	2.6	5.7
Nb	0.35	0.65	0.04	0.05	0.22	0.13	0.22	0.04	1.30	0.19	0.05	0.14	0.45	1.18
Cs	0.04	0.01	0.01	0.01	0.04	0.06	0.02	0.03	0.18	0.07	0.02	0.05	0.08	0.14
Ba	2.58	1.29	0.19	0.81	1.06	13.50	0.73	0.22	10.54	6.10	0.55	1.49	3.94	2.47
La	0.47	0.39	0.06	0.08	0.69	0.19	0.44	0.04	1.41	0.23	0.07	0.10	0.40	1.51
Ce	0.93	0.85	0.11	0.16	1.26	0.37	1.02	0.11	2.99	0.49	0.15	0.22	0.82	2.91
Pr	0.13	0.11	0.02	0.02	0.18	0.06	0.16	0.02	0.43	0.07	0.02	0.03	0.13	0.39
Nd	0.54	0.47	0.08	0.10	0.76	0.26	0.69	0.11	1.78	0.29	0.09	0.15	0.54	1.51
Sm	0.12	0.10	0.02	0.03	0.17	0.08	0.16	0.03	0.39	0.07	0.02	0.04	0.13	0.34
Eu	0.03	0.03	0.005	0.01	0.04	0.02	0.04	0.01	0.12	0.02	0.01	0.01	0.04	0.10
Gd	0.13	0.11	0.02	0.03	0.20	0.07	0.17	0.03	0.39	0.08	0.02	0.05	0.16	0.38
Tb	0.02	0.02	0.004	0.005	0.03	0.01	0.03	0.004	0.06	0.01	0.004	0.01	0.03	0.06
Dy	0.12	0.10	0.02	0.03	0.20	0.06	0.14	0.02	0.33	0.07	0.02	0.05	0.16	0.34
Ho	0.02	0.02	0.004	0.01	0.04	0.01	0.03	0.004	0.06	0.01	0.005	0.01	0.03	0.07
Er	0.06	0.06	0.01	0.02	0.12	0.04	0.07	0.01	0.16	0.04	0.01	0.03	0.09	0.18
Yb	0.06	0.06	0.02	0.02	0.12	0.04	0.07	0.02	0.14	0.04	0.02	0.03	0.09	0.17
Lu	0.01	0.01	0.003	0.003	0.02	0.01	0.01	0.003	0.02	0.01	0.003	0.01	0.01	0.02
Hf	0.06	0.08	0.01	0.01	0.06	0.04	0.06	0.01	0.22	0.04	0.01	0.02	0.08	0.18
Ta	0.02	0.05	0.002	0.003	0.02	0.01	0.01	0.00	0.08	0.01	0.004	0.09	0.08	0.11
Pb	0.3	1.1	0.1	0.1	0.2	0.5	0.1	0.03	0.3	5.6	0.1	0.2	0.1	0.4
Th	0.05	0.1	0.01	0.01	0.1	0.02	0.04	0.01	0.2	0.03	0.02	0.01	0.04	0.1
U	0.01	0.02	0.002	0.02	0.01	0.02	0.01	0.003	0.03	0.01	0.002	0.003	0.01	0.03
Sb	0.01	0.02	0.01	0.04	0.02	0.02	0.01	0.001	0.03	0.04	0.01	0.02	0.02	0.04

Notes: * = ship powder. Boron and Li concentrations were analyzed on the direct-current plasma-atomic emission spectrometer at USF.

Table T4. Shore-based DCP-AES major and trace elements analysis of meta-basic rocks recovered from the Leg 125 Holes 778A and 779A.

Core, section interval (cm):	125-778A-					125-779A-	
	11R-1 6-8	74R-1 16-20	7R-1 1-3	8R-1 3-4	7R-1 1-3	31R-2 100-102	31R-1 117-119
Major element oxide (wt%):							
SiO ₂	49.10	50.02	52.78	46.88	53.66	41.51	47.05
Al ₂ O ₃	9.70	12.65	12.55	5.85	12.61	14.43	0.31
Fe ₂ O ₃ T	11.44	12.53	11.86	3.02	11.82	12.05	7.68
MgO	7.85	10.77	7.10	37.43	6.92	7.46	44.66
MnO	0.17	0.18	0.17	0.28	0.19	0.19	0.15
CaO	9.06	9.37	7.12	3.12	7.16	22.78	0.34
K ₂ O	0.86	0.63	0.59	0.03	0.38	0.06	0.03
Na ₂ O	2.90	1.98	2.79	0.99	5.06	0.19	0.14
TiO ₂	1.12	1.85	2.44	0.41	2.44	1.33	0.00
Totals:	99.64	100.58	100.24	98.02	100.24	100.00	100.32
Trace element (ppm):							
Sr	52.5	56.6	50.6	35.9	51.2	62.1	106
Ba	52.7	35.7	37.4	24.3	37.4	105.1	264.7
Ni	1066	183	45.2	14.2		54.0	1959
Sc	24.2	23.6	23.3	26.2	35.2	56.1	4.8
Cr	1001	118.7	42.7		50.2	202	2274
V	250	312	356	115	383	336	24.5
Zn	116	125	109	234	123	181	83.3
Cu	56	21	38	564	61	86	5
Co	61	54	53	75	53	68	

Table T5. Shore-based DCP-AES major and trace elements analysis of metabasic rocks recovered from the Leg 195 Holes 1200B, 1200D, and 1200F.

Core, section interval (cm):	195-1200B		195-1200D		195-1200F		
	Talc schist	Chlorite- amphibole schist	8H-1 115-120	8H-1 119-121	1H-5 18-20	2H-2 3-5	2H-3 90-92
Major element oxide (wt%):							
SiO ₂	49.92	45.94	30.73	36.45	53.41	63.56	45.04
Al ₂ O ₃	12.10	9.28	22.91	22.47	2.78	12.45	2.57
Fe ₂ O ₃ T	9.79	12.20	15.24	12.47	4.16	6.32	9.31
MgO	14.77	22.17	3.54	3.53	17.16	8.25	40.65
MnO	0.18	0.30	0.21	0.18	0.16	0.10	0.17
CaO	9.89	6.49	23.04	22.05	21.69	3.64	0.18
K ₂ O	0.37	0.18	0.01	0.01	0.03	0.51	0.04
Na ₂ O	2.00	2.31	0.75	0.59	0.61	3.58	0.56
TiO ₂	0.97	1.12	3.58	3.28	0.04	0.17	0.01
Totals:	100.00	100.00	100.00	101.02	100.00	98.58	98.59
LOI	5.4	10.5	7.5	7.4	2.2	13.7	19.4
Trace element (ppm):							
Sr	121	63.07	35.3	326	54.4	204	345
Ba	11.48	26.41	57.8	46.8	15.9	9.9	356
Ni	1184	1887	1434		7610	42.3	2.0
Sc	26.91	27.38	31.1	129	14.1		45.4
Cr	339	344	1182		3950	1036	39
V	118	171	78.3	1672	50.3		248
Zn	120	146	155		56		217
Cu	11	46	10	196	26		24
Co	54	66	64			28	55

Note: LOI = loss on ignition.

Table T6. Shore-based DCP-AES major and trace elements analysis of metabasic rocks recovered from the Leg 195 Holes 1200B, 1200D, and 1200F.

Core, section, interval (cm)	Trace element (ppm)		
	B	Be	Li
125-778A-			
4R-1, 16–20	28.4		5.6
11R-1, 6–8 (Breccia)	49.5	0.44	
4R-1, 16–20	28.4	0.18	8.6
8R-1, 3–4	14.8	1.80	
7R-1, 1–3	33.5	2.38	11.0
125-779A-			
31R-2, 100–102	30.9	0.10	7.2
31R-1, 117–119	26.9	0.04	20.2
195-1200B-			
Talc schist		1.36	5.6
Talc schist*		0.92	5.3
Chlorite-amphibole schist		2.24	16.3
Mica schist		0.25	
195-1200D-			
8H-1, 115–120	41.8	8.10	20.5
8H-1, 119–121	50.4	4.85	17.7
8H-1, 119–121*		3.33	18.0
195-1200F-			
1H-4, 6–8		0.41	0.3
1H-5, 18–20	25.2	0.17	10.2
1H-5, 18–20*		0.16	9.5
2H-2, 3–5	10.8	0.10	55.5
2H-2, 3–5*		0.05	58.2
2H-3, 90–92	60.8	0.02	18.9

Note: * = duplicate analysis was performed on sample.

Table T7. ICP-MS analysis of metabasic rocks recovered from the ODP Legs 125 and 195.

Core, section interval (cm):	195-1200B	195-1200D	195-1200F			125-779A	
	Wash core, talc schist	8H-1 119-121	1H-5 18-20	2H-2 3-5	2H-3 90-92	31R-1 117-119	31R-2 100-102
Depth (mbsf):		26.19	6.18	9.23	10.41	247.66	249.50
Trace element (ppm):							
Li (DCP)	5.6	17.7	10.2	55.5	18.9		
Li (ICP-MS)	5.3	18.0	9.5	58.2	18.9		
Be (DCP)	1.36	4.85	0.17	0.10	0.02		
Be (ICP-MS)	0.92	3.33	0.16	0.1	0.02		
Sc	22.5	14.0	5.7	33.6	11.0		
Cu	2.6	16.2	1.8	55.9	25.8		
Zn	53.5	159	23.3	113	31.3		
As	0.4	2.6	5.1	0.6	2.6		
Rb	0.2	0.3	0.0	1.6	3.8	0.12	0.30
Sr	9.1		31.6	28.5	48.7		
Y	9	39	2	25	6	31.4	28.5
Zr	8.2		0.9		0.2		
Nb	1.4		0.4	6.4	0.03		
Sb	0.1	0.4	0.3	0.1	0.2		
Cs	0.05	0.2	0.01	0.8	2.7		
Ba	0.8	203.1	25.5	9.8	11.1		
La	1.1	68.6	2.6	7.3	0.5	3.1	3.0
Ce	3.2		3.1	18.6	1.1	10.0	9.4
Pr	0.7	20.3	0.4	3.0	0.2	1.8	1.7
Nd	3.5	81.2	1.4	13.7	0.9	10.4	9.6
Sm	1.1	15.5	0.3	3.8	0.3	3.4	3.1
Eu	0.3	4.6	0.1	0.8	0.1	1.2	1.1
Gd	1.3	13.5	0.3	4.5	0.5	4.5	4.2
Tb	0.2	2.0	0.05	0.8	0.1	0.8	0.7
Dy	1.3	9.4	0.2	4.6	0.6	5.5	5.0
Ho	0.3	1.5	0.1	0.9	0.1	1.2	1.1
Er	0.8	3.7	0.2	2.3	0.4	3.6	3.3
Yb	0.8	2.5	0.2	1.9	0.3	3.5	3.1
Lu	0.1	0.3	0.04	0.2	0.04	0.5	0.5
Hf	0.4	11.9	0.03	2.8	0.01		
Ta	0.1	3.8	0.03	0.4	0.004		
Pb	0.8	3.6	0.8	0.2	0.4	0.3	0.2
Th	0.2	5.9	0.2	0.3	0.001	0.1	0.1
U	0.0	1.2	0.0	0.1	0.001	0.1	0.1

Notes: Note the good agreement for Li and Be in the DCP-AES (USF) and ICP-MS (BU) datasets. DCP = direct current plasma, ICP-MS = inductively coupled plasma-mass spectroscopy.

Table T8. Selected average element concentrations.

Element	Average metamorphic schist	Average serpentinized peridotite	Average serpentinite mud
Yb (ppm)	1.76	0.01	0.06
Th (ppm)	1.30	0.001	0.04
Nd (ppm)	17.24	0.01	0.44
Sc (ppm)	17.36	6.00	5.83
Ba (ppm)	50.05	2.11	2.73
Rb (ppm)	1.18	0.74	0.32
Al ₂ O ₃ (wt%)	10.90	0.57	0.93

Note: Concentrations were used in calculating mixing lines between serpentinized peridotites and metamorphic schists (Figure F15, p. 34). Serpentinized peridotite data from Salisbury, Shonohara, Richter, et al. (2002) and Savov et al. (2004).

CHAPTER NOTE*

- N1. Fryer, P., Gharib, J., Ross, K., Savov, I.P., and Mottl, M.J., submitted. Origins of serpentinite muds from Mariana forearc seamounts. *Earth Planet. Sci. Lett.*